

Evolving antibody response to SARS-CoV-2 antigenic shift from XBB to JN.1

<https://doi.org/10.1038/s41586-024-08315-x>

Received: 18 June 2024

Accepted: 30 October 2024

Published online: 7 November 2024

Open access

 Check for updates

Fanchong Jian^{1,2,3,11}, Jing Wang^{1,2,4,11}, Ayijiang Yisimayi^{1,2,4,11}, Weiliang Song^{1,2,4,11}, Yanli Xu^{5,11}, Xiaosu Chen⁶, Xiao Niu^{1,3}, Sijie Yang^{1,7}, Yuanling Yu², Peng Wang², Haiyan Sun², Lingling Yu², Jing Wang², Yao Wang², Ran An², Wenjing Wang², Miaomiao Ma², Tianhe Xiao^{1,8}, Qingqing Gu², Fei Shao², Youchun Wang^{2,9}, Zhongyang Shen¹⁰, Ronghua Jin⁵ & Yunlong Cao^{1,2,7}✉

The continuous evolution of SARS-CoV-2, particularly the emergence of the BA.2.86/JN.1 lineage replacing XBB, necessitates re-evaluation of vaccine compositions^{1–3}. Here, we provide a comprehensive analysis of the humoral immune response to XBB and JN.1 human exposure. We demonstrate the antigenic distinctiveness of XBB and JN.1 lineages in SARS-CoV-2-naïve individuals and show that infection with JN.1 elicits superior plasma neutralization against its subvariants. We highlight the strong immune evasion and receptor-binding capability of KP.3, supporting its foreseeable prevalence. Extensive analysis of the B cell receptor repertoire, in which we isolate approximately 2,000 receptor-binding-domain-specific antibodies, with targeting epitopes characterized by deep mutational scanning, underscores the superiority of JN.1-elicited memory B cells^{4,5}. Class I IGHV3-53/3-66-derived neutralizing antibodies (NAbs) are important contributors to the wild-type reactivity of NAbs against JN.1. However, KP.2 and KP.3 evade a substantial subset of these antibodies, even those induced by JN.1, supporting a need for booster updates. JN.1-induced Omicron-specific antibodies also demonstrate high potency across Omicron. Escape hotspots for these NAbs have already been mutated, resulting in a higher immune barrier to escape and indicating probable recovery of escaped NAbs. In addition, the prevalence of IGHV3-53/3-66-derived antibodies and their ability to compete with all Omicron-specific NAbs suggests that they have an inhibitory effect on the activation of Omicron-specific naïve B cells, potentially explaining the heavy immune imprinting in mRNA-vaccinated individuals^{6–8}. These findings delineate the evolving antibody response to the antigenic shift of Omicron from XBB to JN.1 and highlight the importance of developing the JN.1 lineage, especially KP.2- and KP.3-based vaccine boosters.

Since the emergence of the SARS-CoV-2 BA.2.86 lineage in July 2023, its subvariants, especially JN.1, have continued to circulate and evolve rapidly, outcompeting the previously prevalent XBB subvariants^{1,3,9–11}. By June 2024, the JN.1 lineage accounted for more than 93% of newly observed sequences (Fig. 1a). BA.2.86 and JN.1 have convergently accumulated mutations on the receptor-binding domain (RBD) of the viral spike glycoprotein, including R346S/T, F456L/V and A475V/S^{12,13} (Extended Data Fig. 1a). A newly detected subvariant, designated KP.3, even carries an unprecedented Q493E mutation^{14,15}. Most of these sites mutated in JN.1 subvariants are located near the receptor-binding motif (RBM) (Extended Data Fig. 1b). This means there is a crucial need to investigate the abilities of these subvariants to evade the current humoral immune barrier established by SARS-CoV-2 infections and vaccines.

Previous studies have demonstrated that JN.1-effective neutralizing antibodies (NAbs) can be elicited by XBB-based vaccine boosters^{2,16,17}. However, considering the extensive mutations carried by JN.1, it is important to investigate whether JN.1 immunization performs substantially better against current and potential future variants^{1,3,18}. Here, we provide a systematic comparison of the humoral immune response between XBB and JN.1 lineages in human infections at both serum and memory B cell (MBC)-encoded antibody resolution.

Immunogenicity of JN.1 exposure

To evaluate the antigenicity and immunogenicity of the XBB and JN.1 lineages, we first administered a two-dose immunization of variant spike

¹Biomedical Pioneering Innovation Center (BIOPIC), Peking University, Beijing, China. ²Changping Laboratory, Beijing, China. ³College of Chemistry and Molecular Engineering, Peking University, Beijing, China. ⁴School of Life Sciences, Peking University, Beijing, China. ⁵Beijing Ditan Hospital, Capital Medical University, Beijing, China. ⁶Institute for Immunology, College of Life Sciences, Nankai University, Tianjin, China. ⁷Peking-Tsinghua Center for Life Sciences, Tsinghua University, Beijing, China. ⁸Joint Graduate Program of Peking-Tsinghua-NIBS, Academy for Advanced Interdisciplinary Studies, Peking University, Beijing, China. ⁹Institute of Medical Biology, Chinese Academy of Medical Science & Peking Union Medical College, Kunming, China. ¹⁰Organ Transplant Center, NHC Key Laboratory for Critical Care Medicine, Tianjin First Central Hospital, Nankai University, Tianjin, China. ¹¹These authors contributed equally: Fanchong Jian, Jing Wang, Ayijiang Yisimayi, Weiliang Song, Yanli Xu. ✉e-mail: yunlongcao@pku.edu.cn

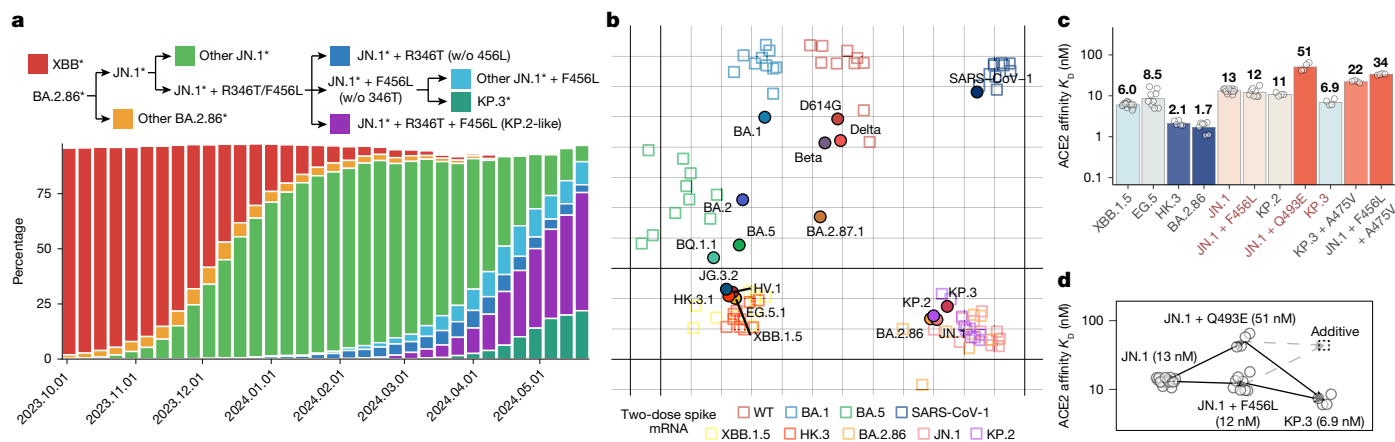


Fig. 1 | Antigenicity and receptor binding of emerging JN.1 subvariants. **a**, Dynamics of the percentages of XBB and JN.1 lineages in GISAID sequences from September 2023 to June 2024. **b**, Antigenic cartography of mouse sera neutralization data with SARS-CoV-2 variant spike vaccination. Each square indicates a plasma sample, and each circle indicates a SARS-CoV-2 variant.

mRNA to naive mice (Extended Data Fig. 2a). We observed a pronounced distinction in antigenicity between the XBB and JN.1 lineages (Fig. 1b and Extended Data Fig. 2b). Notably, within the JN.1 family, KP.3 showed a considerable difference in antigenicity compared with JN.1 and KP.2, even when mice were immunized with KP.2 spike. These differences in antigenicity, at least in naive mice, could prompt consideration of changing SARS-CoV-2 vaccine compositions from XBB to JN.1 families.

Future SARS-CoV-2 variant prevalence provides critical guidance for vaccine composition assessment. The human ACE2 (hACE2)-binding affinity of viral RBDs is highly related to viral fitness, and previous studies have reported a synergistic impact of RBD L455–F456 mutations on ACE2 receptor-binding affinity mediated by Q493 (refs. 12,19–22). As these sites are also convergently mutated in BA.2.86 lineages, especially JN.1, we tested the binding affinities of JN.1 subvariant RBDs to hACE2 using surface plasmon resonance (SPR) (Extended Data Fig. 1c). L455S in JN.1 dampened the high affinity of the BA.2.86 RBD, as shown previously^{1,23}. Notably, F456L and R346T + F456L did not greatly affect the hACE2-binding affinity of JN.1, whereas the Q493E mutation of KP.3 substantially improved receptor-binding affinity on the basis of JN.1 + F456L (Fig. 1c and Extended Data Fig. 1d). Notably, Q493E alone significantly reduced ACE2-binding affinity in the context of JN.1 RBD but unexpectedly enhanced the affinity when combined with the F456L mutation, indicating non-additive epistatic interactions^{12,24,25} (Fig. 1d). The high affinity of KP.3, achieved through epistasis, may enable incorporation of A475V for further immune evasion (Fig. 1c). Overall, this extraordinary ACE2-binding affinity may bolster the rapid transmission and prevalence of KP.3, enhancing its potential to acquire further immune-evasive mutations.

Human serum antibody evasion is the most decisive factor in SARS-CoV-2 viral fitness. To analyse the humoral immune evasion capability and immunogenicity of JN.1 lineages, we collected blood samples from eight cohorts, including individuals infected by XBB* (asterisk denotes this strain and all of its subvariants; $n = 11$) or JN.1 ($n = 4$) without known previous exposure to SARS-CoV-2; those who experienced XBB infection after three doses of inactivated vaccines; those who experienced sequential infections of BA.5/BF.7 and XBB* ($n = 14$), or BA.5/BF.7 and JN.1 ($n = 29$); and those who received three-dose inactivated vaccines followed by BA.5/BF.7 breakthrough infection (BTI) and were then reinfected by XBB (mainly XBB + S486P), HK.3 or JN.1 ($n = 54$, 18 and 29, respectively) (Fig. 2a and Extended Data Fig. 3).

Priming with XBB and JN.1 in naive humans elicited distinct NABs without observable cross-lineage reactivity; this confirms that XBB

c, Bar plots showing the affinities of SARS-CoV-2 variants determined by SPR. Each circle indicates a replicate. Geometric mean K_D (nM) values are indicated by the height of bars and annotated above each bar. **d**, Schematic of the non-additive impacts of ACE2 binding between F456L and Q493E. The dashed grey arrows show the additive results. w/o, without.

and JN.1 are antigenically distinct in both human and mice, indicating that antigenic change from XBB to JN.1 lineage results in different serotypes^{26,27} (Fig. 2b). By contrast, a previous BA.5 (or BF.7, omitted hereafter) infection improved the cross-lineage reactivity of antibodies induced by XBB or JN.1 reinfection. This suggests that BA.5 priming could induce Omicron cross-reactive NABs that are effective against both XBB and JN.1 lineages (Fig. 2c).

Notably, in the three BTI with reinfection cohorts, BA.5 BTI + XBB infection elicited the lowest 50% neutralization titre (NT_{50}) against JN.1 lineage variants (Fig. 2d). On average, JN.1 reinfection induced 5.9-fold higher NT_{50} against JN.1, 4.9-fold higher NT_{50} against KP.2 and 4.8-fold higher NT_{50} against KP.3, compared with XBB reinfection (Fig. 2e). The improvement of JN.1 BTI over HK.3 BTI was less significant, possibly owing to the shorter interval between two infections in the XBB reinfection cohort, in addition to the immunogenicity drift attributed to the ‘FLip’ mutations (L455F + F456L) of HK.3. Among all five reinfection cohorts, all of the four tested JN.1 subvariants with RBD mutations (JN.1 + R346T, JN.1 + F456L, KP.2 and KP.3) exhibited notable immune evasion. KP.3 was consistently the strongest escaper, leading to a 1.9- to 2.4-fold reduction in NT_{50} compared with JN.1. Notably, a recently emerged deletion on N-terminal domain S31, which leads to N30 glycosylation and was convergently detected in multiple independent JN.1 sublineages including KP.2.3, LB.1, KP.3.1.1 and LF.2, resulted in further antibody evasion in all cohorts²⁸ (Fig. 2c,d and Extended Data Fig. 3).

Antigenic cartography of our human plasma neutralization data was used to visualize the antigenic differences among SARS-CoV-2 variants. The antigenic map from single-exposure cohorts clearly depicted the intrinsic antigenic distances between XBB and JN.1 lineages in humans, despite sample size limitations (Fig. 2f). Samples from BTI with reinfection cohorts showed strong ancestral strain imprinting, indicated by the aggregation of points near the D614G strain (Fig. 2g). Nevertheless, the JN.1 BTI cohorts had closer distances to current circulating variants, supporting the idea of switching vaccine boosters to JN.1 lineages.

Together, these observations underscore the significant antigenic distinctions between the SARS-CoV-2 XBB and JN.1 lineages and highlight the notable ACE2 affinity and NAB-escaping capability of emerging JN.1 subvariants, especially KP.3 and KP.3 + S31del (KP.3.1.1), supporting their foreseeable prevalence. The results provide phenomenological but compelling evidence to shift the focus of vaccine booster strategies from XBB to JN.1 lineages, ideally KP.3.

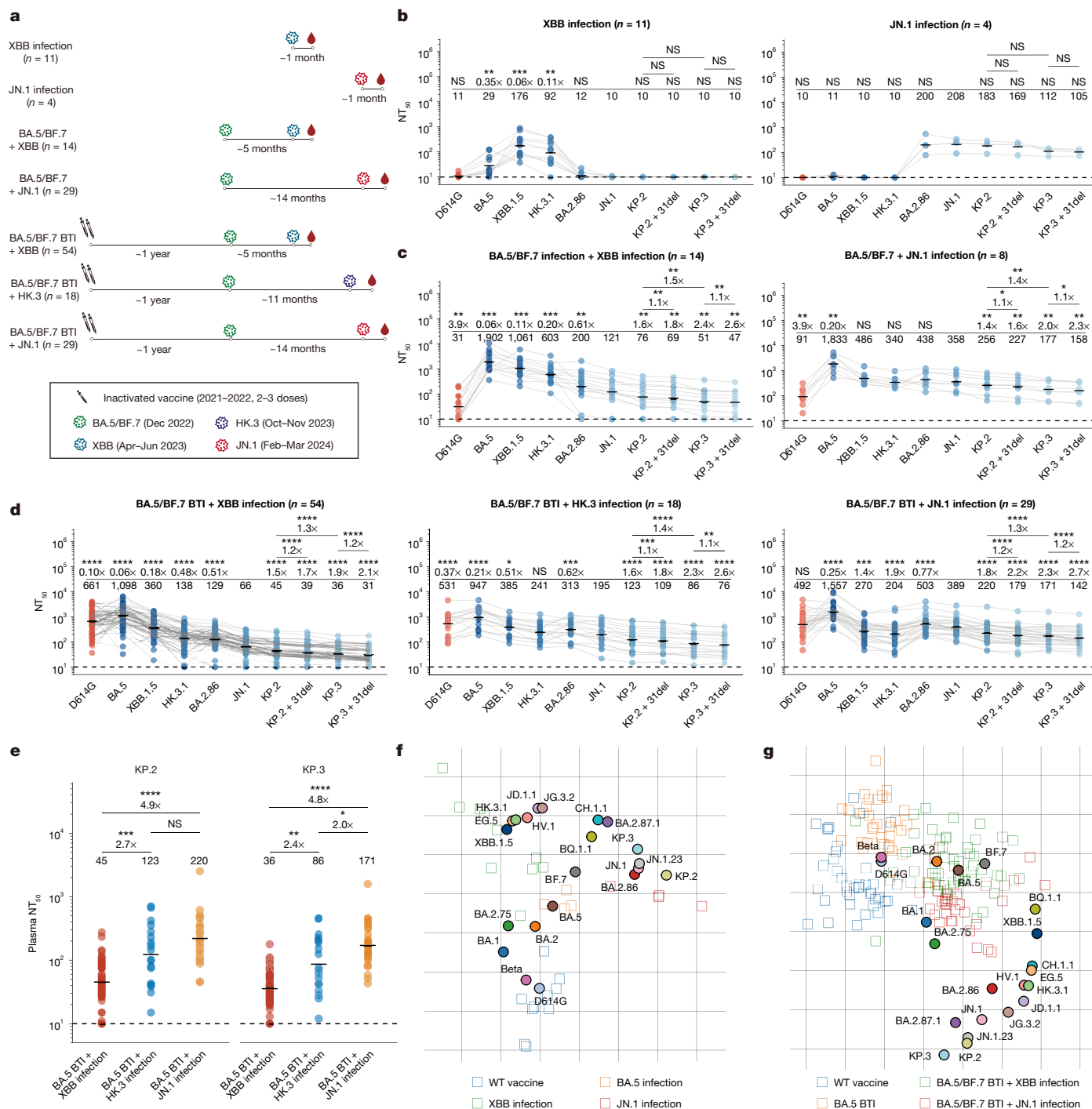


Fig. 2 | Antigenicity and immunogenicity comparison of XBB and JN.1 lineages in human. **a**, Schematic of the SARS-CoV-2-related immune histories of the seven cohorts involved in this study. **b–d**, NT_{50} values of plasma samples from human cohorts with XBB or JN.1 single infection (**b**), XBB or JN.1 infection with previous BA.5 or BF.7 infection (**c**) and XBB, HK.3 or JN.1 infection with previous vaccination and BA.5 or BF.7 infection (**d**) against SARS-CoV-2 variant pseudoviruses. Plasma source cohorts and corresponding number of samples are labelled above each panel. Dashed lines indicate the limit of detection ($NT_{50} = 10$). Numbers of negative samples are labelled below the dashed lines. Geometric mean titre (GMT) values are labelled as black bars and shown above

each group of points, with fold changes and significance compared with JN.1. Two-tailed Wilcoxon signed-rank tests were used to calculate the P values. **e**, Comparison of neutralization of plasma samples from three BTI + reinfection cohorts against KP.2 and KP.3. GMT values are labelled as black bars and above the points, with pairwise fold changes shown. Two-tailed Wilcoxon rank-sum tests were used to determine the P values. **f, g**, Antigenic cartography was performed using human plasma neutralization data of single-exposure cohorts (**f**) or ancestral strain imprinted cohorts (**g**). Each square indicates a plasma sample, and each circle indicates a SARS-CoV-2 variant. * $P < 0.05$; ** $P < 0.01$; *** $P < 0.001$; **** $P < 0.0001$; NS, not significant.

JN.1-induced MBC repertoire

Next, we aimed to determine the specific molecular constituents responsible for the broad-spectrum neutralization observed in

plasma polyclonal antibodies elicited by infections with the JN.1 lineage, to understand how previous vaccination or infection with BA.5 facilitates the development of cross-lineage NAbs following infection with XBB/JN.1. Analysis of the MBC repertoire could also help

to predict the response to future variant exposures. Consequently, it is imperative to clarify the roles of antibodies that exhibit diverse cross-reactivities and target multiple epitopes, particularly on the virus RBD, the most immunogenic domain targeted by NAbS. We used fluorescence-activated cell sorting (FACS) to isolate RBD-specific CD20⁺ CD27⁺ IgM⁻ IgD⁻ B cells from the peripheral blood mononuclear cells (PBMCs) of the human donors mentioned above. We used variant RBDs (XBB.1.5, HK.3 or JN.1) corresponding to the last-exposure SARS-CoV-2 strain for each cohort in the sorting (Supplementary Information Fig. 1). Following our previously established methodology, we determined the sequences of the monoclonal antibody (mAb) heavy and light chain variable domains using single-cell V(D)J sequencing and expressed them as human IgG1 (refs. 4, 5, 8, 29, 30). The resultant mAbs were characterized using enzyme-linked immunosorbent assays (ELISAs) to assess their binding specificities against the wild type (WT) and the corresponding Omicron RBDs.

BA.5 BTI + reinfection consistently induced higher plasma neutralization titres against BA.5 compared with D614G, demonstrating the substantial contribution of Omicron-specific NAbS (Fig. 2d). This was validated by mAb analyses, consistent with our earlier discovery that repeated Omicron infections may mitigate the imprinting of inactivated vaccines based on the ancestral strain⁸. However, recent research involving individuals who had undergone Omicron reinfection after receiving mRNA vaccines based on the ancestral strain found pronounced immune imprinting; as a result, Omicron-specific MBCs were scarcely detectable even after two exposures to Omicron^{6,7,31}. The XBB BTI cohort, comprising convalescents who had undergone a single Omicron exposure postvaccination, exhibited the highest proportion (62%) of RBD-specific mAbs that cross-reacted with the WT. Some vaccine-naïve cohorts, including XBB infection, BA.5 + XBB infection and BA.5 + JN.1 infection, also generated 40–50% WT-reactive antibodies. The BA.5 + JN.1 infection cohort induced a higher percentage of WT-reactive mAbs compared with the BA.5 BTI + JN.1 infection cohort (Fig. 3a). However, the corresponding plasma samples did not show elevated neutralization titres against the D614G pseudovirus, suggesting enrichment of cross-reactive mAbs that target non-neutralizing epitopes (Fig. 2c).

We observed substantial variations in V(D)J gene usage among mAbs with different reactivities to WT and those elicited by different immune histories. In the BA.5 BTI + reinfection cohorts, WT-reactive mAbs showed prominent usage of IGHV3-53 and IGHV3-66, which are recognized as part of the public immune response, with predominantly class I NAbS targeting the RBM^{30,32}. However, mAbs of these types are scarcely seen in cohorts without vaccination, in which there is higher utilization of IGHV5-51 and IGHV4-39 (Extended Data Fig. 4a). Regarding Omicron-specific mAbs, IGHV2-5 was prevalent across all cohorts; however, it was not dominant among JN.1-infected convalescents, who showed higher proportions of mAbs derived from IGHV5-51 (Extended Data Fig. 4b). Notably, IGHV5-51 is extensively used in WT-reactive antibodies, underscoring its significance, particularly in the context of JN.1 infections.

As expected, rates of somatic hypermutation (SHM) in both the heavy and light chains of mAbs were closely associated with the number of antigen exposures. Specifically, WT-reactive mAbs exhibited more SHMs than Omicron-specific mAbs in vaccinated individuals but not in unvaccinated ones. The BA.5 BTI + HK.3/JN.1 cohort generated Omicron-specific mAbs with higher SHM rates compared with the BA.5 BTI + XBB cohort; this was probably due to the longer interval between two Omicron exposures in the former group, which enabled further maturation of Omicron-specific B cells initiated by BA.5 infections (Fig. 3b and Extended Data Fig. 4c).

Generally, Omicron-specific mAbs demonstrated superior neutralization activities compared with WT-reactive mAbs against the JN.1, KP.2 and KP.3 variants. mAbs induced by XBB infection and XBB BTI had very low percentages of potent NAbS, consistent with their

low plasma neutralization titres (Fig. 2a and Extended Data Fig. 3a). Notably, BA.5 + JN.1 and BA.5 BTI + JN.1 infections elicited 30% and 60% JN.1-effective WT-reactive NAbS, respectively, whereas the proportion of effective Omicron-specific mAbs exceeded 90% in both cohorts, surpassing those observed in XBB/HK.3 reinfections (Extended Data Fig. 4d). These findings further substantiate the potential benefits of developing vaccine boosters based on the JN.1 lineages.

Epitope mapping of JN.1-induced mAbs

Despite the promising neutralization activities of JN.1-elicited mAbs, antibodies targeting various epitopes may be evaded by diverse RBD mutations, suggesting their potential vulnerability to future viral antigenic drift. To examine the epitope distribution of mAbs elicited by different immune histories, we conducted high-throughput yeast-display-based deep mutational scanning (DMS) assays to analyse the escape mutation profiles of the isolated mAbs. Specifically, we constructed mutant libraries on the basis of the XBB.1.5 and JN.1 RBDs. We initially assessed the expression levels of these mutants on the yeast surface using FACS followed by sequencing (Sort-seq)^{14,15,33} (Extended Data Fig. 5a–d). Notably, expression of the JN.1 RBD seemed to be more tolerant to mutations compared with that of the BA.2 RBD, yet it was less tolerant than expression of the XBB.1.5 RBD (Extended Data Fig. 5e). We then conducted DMS of mAb-binding capabilities to identify the escape mutations for each mAb and map their targeting epitopes⁸. We successfully assayed the escape mutation profiles of a total of 2,688 mAbs, on the basis of at least one of the two RBD variants, including 1,874 isolated from XBB/JN.1 infection cohorts involved in this study and 814 mAbs previously identified for comparison^{5,8,34,35} (Extended Data Fig. 6a).

We identified 22 mAb clusters, and the corresponding epitope groups for each cluster were annotated on the basis of our previous definitions (Fig. 3c and Extended Data Fig. 6b)^{5,8}. In brief, epitope groups A1/A2 (class 1 (refs. 32, 36)) B (class 1/2, similar to COV2-2196 (ref. 37) and REGN10933 (ref. 38)), D2/D3/D4 (similar to REGN10987 (ref. 38) and LY-CoV1404 (ref. 39)) and F3 (class 1/4, similar to SA55 (ref. 40) and ADG-2/VYD222 (ref. 41)) generally competed with ACE2 and had greater potential to effectively neutralize the virus. Conversely, groups E1/E2 (class 3, S309-like), E3 (also referred to as class 5, S2H97-like⁴²) and F1 (class 4, S304-like) were less likely to compete with ACE2 and did not exhibit potent neutralization (Fig. 3d and Extended Data Fig. 6c,d). Notably, we discovered a subgroup of F1, designated F1.2, which targets an epitope that is adjacent to the traditional F1.1 but slightly closer to the RBM (Extended Data Fig. 6e).

We observed that the proportion of A1 mAbs was correlated with the number of SARS-CoV-2 exposures, reaching its highest levels in cohorts that experienced BTI followed by reinfection (Fig. 3e). These antibodies were notably absent in cases of XBB infection alone, underscoring the importance of initial exposure to earlier variants for the development of such mAbs. By differentiating F1.2 from F1.1, we deduced that WT-based vaccination is essential for eliciting traditional F1.1 non-neutralizing antibodies. By contrast, immunization solely with Omicron induced F1.2 mAbs only, possibly owing to the immunogenicity shift caused by Omicron mutations at RBD positions 371–376. We also noted that JN.1 infections did not elicit E1/E2 mAbs; this could be attributed to N354 glycosylation resulting from K356T in the BA.2.86 lineage. Among the epitope groups, A1, D2, E1/E2/E3 and F1.1 were predominantly cross-reactive to WT, whereas A2, B, D3/D4, F1.2 and F3 primarily consisted of Omicron-specific mAbs (Fig. 3f). Groups F3, A1, B and D3 encompassed potential broadly neutralizing antibodies (bnAbs) against JN.1 subvariants, whereas A2, D2, D4 and E1/E2.1 were largely escaped (Fig. 3g). E2.2/E3/F1.1 typically represent broadly reactive non-neutralizing antibodies. However, the novel F1.2 mAbs, which exhibited weak neutralization against SARS-CoV-2 variants before BA.2.86, demonstrated unprecedentedly enhanced potency

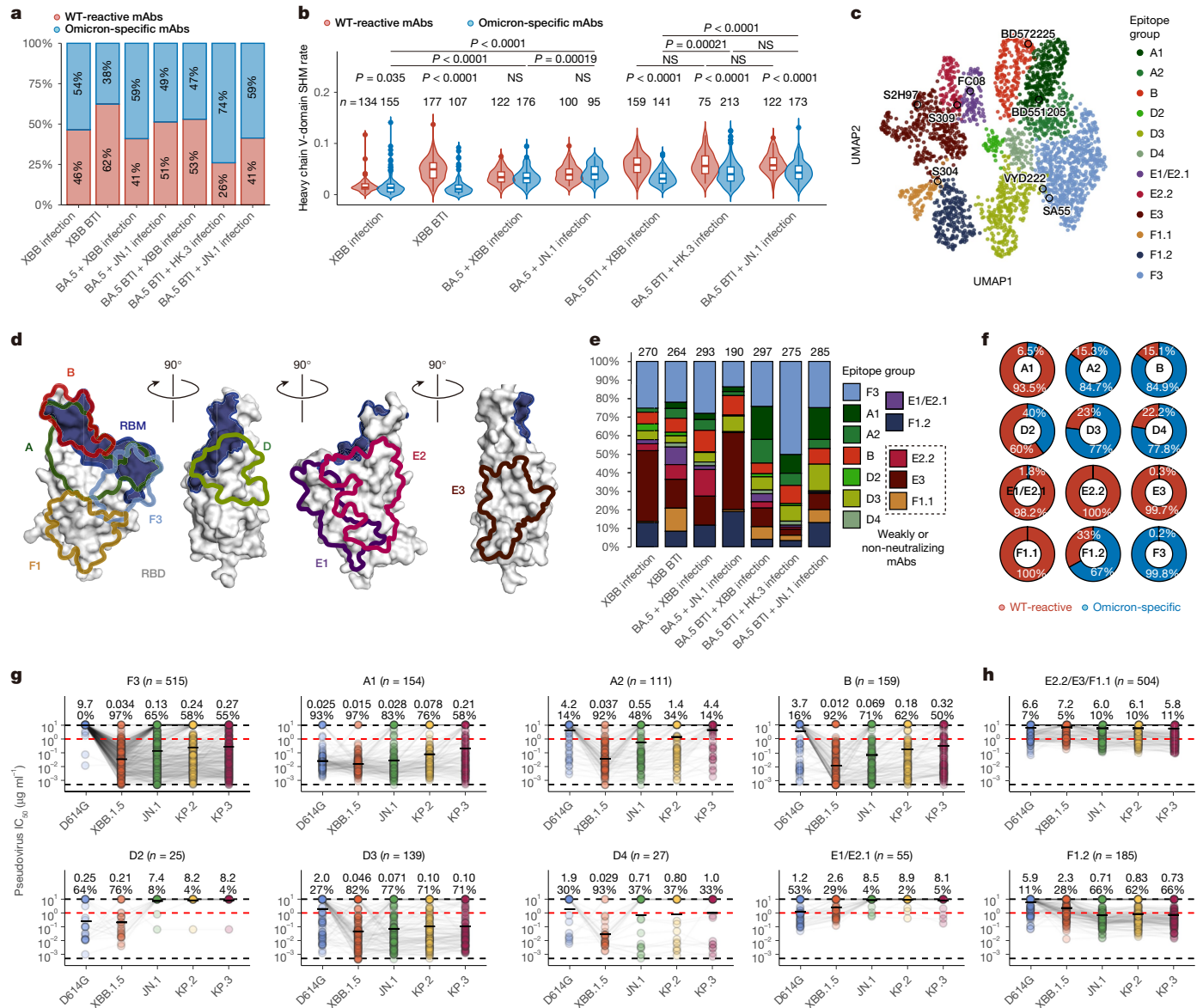


Fig. 3 | Detailed characterization of XBB/JN.1-elicited mAbs. **a**, Proportions of WT-reactive and Omicron-specific mAbs isolated from different cohorts. Antibody reactivities were determined by ELISA against SARS-CoV-2 WT RBD and XBB.1.5, HK.3, or JN.1 RBD corresponding to the last-exposure variant. **b**, Distribution of heavy chain SHM rate of WT-reactive and Omicron-specific antibodies isolated from different cohorts. Numbers of mAbs are annotated above each violin plot. Two-tailed Wilcoxon rank-sum tests were used to calculate the *P* values. **c**, Uniform manifold approximation and projection (UMAP) visualization of antibody DMS escape mutation profiles. Well-known mAbs are highlighted by circles with names annotated. **d**, Schematic of the

targeting sites of each epitope group on RBD. Epitope groups targeting spatially overlapping epitopes have been merged. **e**, Percentage of mAbs from each cohort in each epitope group. Numbers of epitope-characterized mAbs are labelled above the bars. **f**, Percentages of WT-reactive and Omicron-specific mAbs in each epitope group. **g, h**, Neutralization activities in IC_{50} of mAbs in epitope groups A1, A2, B, D2, D3, D4, E1/E2.1 and F3 (**g**) and groups E2.2, E3, F1.1 and F1.2 (**h**) against D614G, XBB.1.5, JN.1, KP.2 and KP.3 pseudovirus. Numbers of mAbs in each group are shown in subtitles. Geometric mean IC_{50} values ($\mu\text{g ml}^{-1}$) and percentages of mAbs with $IC_{50} < 1 \mu\text{g ml}^{-1}$ are labelled above each group of points.

against JN.1 lineages (Fig. 3h). In addition, groups E1/E2.1, E2.2, F1.1 and F1.2 showed significant preference for light chain V genes, enriching for IGLV1-40, IGLV3-21, IGKV1-39 and IGLV6-57, respectively. Furthermore, E1/E2.1 and F1.1 tended to use the IGHV1-69 and IGHV3-13/3-30 heavy chains, respectively, to pair with the corresponding light chains (Extended Data Fig. 6f).

Class 1 mAbs dominate WT-reactive bnAbs

Given the potential scarcity of Omicron-specific NAbs within the mRNA-vaccinated population, we next focused on the properties of WT-reactive mAbs elicited by three BA.5 BTI + reinfection cohorts.

Consistent with the plasma neutralization and overall mAb neutralization analyses described above, WT-reactive mAbs from HK.3 and JN.1 infections were significantly more effective than those from XBB infection against JN.1, KP.2 and KP.3 (Fig. 4a). We then calculated the ‘effectiveness scores’ for each epitope group from each source cohort, defined as the number of mAbs in each epitope group weighted by their half-maximal inhibitory concentration (IC_{50}) values against a specific variant. This metric helped us to discern the contribution of each epitope group to neutralization (Fig. 4b). Notably, epitope group A1 consistently made a major contribution to effectiveness against not only JN.1 but also KP.2 and KP.3, which accumulate multiple mutations on the A1 epitope or even its escape

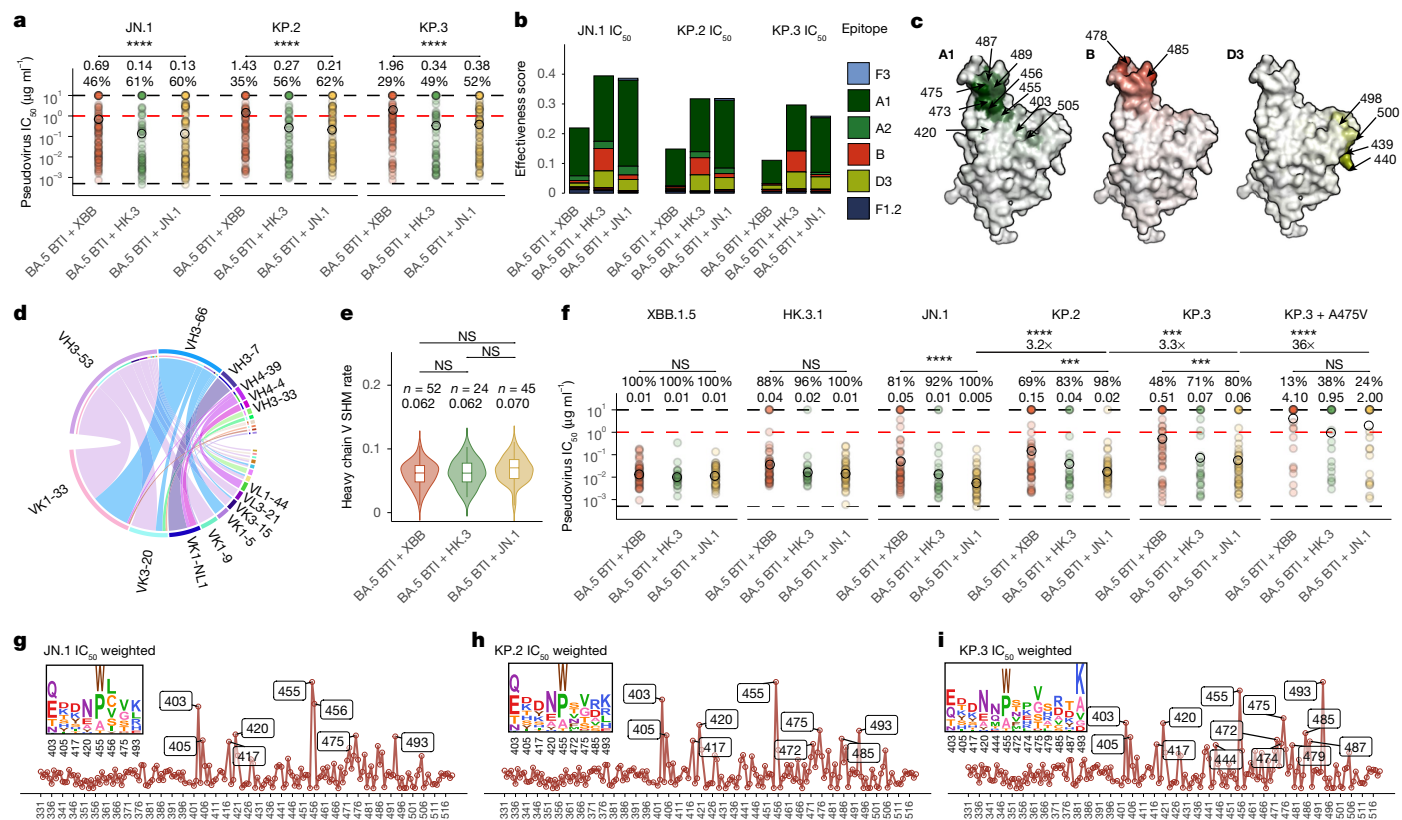


Fig. 4 | Class 1 dominates WT-reactive bnAbs. **a**, Neutralization activities of WT-reactive mAbs isolated from three BTI + reinfection cohorts against JN.1, KP.2 and KP.3. Geometric mean IC_{50} values ($\mu\text{g ml}^{-1}$) and percentages of mAbs with $IC_{50} < 1 \mu\text{g ml}^{-1}$ are labelled above each group of points. **b**, Stacked bar charts showing the effectiveness scores of WT-reactive mAbs in each epitope group weighted by IC_{50} against JN.1, KP.2 and KP.3. **c**, Average DMS site escape scores of mAbs in epitope groups A1, B and D3. Hotspot residues are indicated by arrows. **d**, Chord diagram showing the heavy-light chain V gene pairing of mAbs in epitope group A1. The names of corresponding germline genes are annotated next to the strips. **e**, Comparison of heavy chain SHM rates of A1 mAbs elicited by BA.5 BTI + XBB, HK.3 and JN.1 reinfection cohorts.

hotspots, including L455S, F456L and Q493E (Fig. 4b,c and Extended Data Fig. 6d).

As mentioned above, group A1 or class 1 mAbs are predominantly derived from the IGHV3-53 and IGHV3-66 germlines, which are well known as part of the public immune response^{30,32,43,44}. These mAbs tend to pair with the IGKV1-33 and IGKV3-20 light chain. A specific subset from the BA.5 BTI + XBB reinfection cohort uses IGHV3-7 with IGKV1-NL1. The WT-reactive A1 mAbs from the three BTI + reinfection cohorts exhibited similar heavy chain SHM rates and neutralizing activities against XBB.1.5 and HK.3.1 (Fig. 4e,f). Nonetheless, those elicited by HK.3 and JN.1 demonstrated significantly enhanced neutralization against JN.1 subvariants. Notably, KP.2 and KP.3 evaded ($IC_{50} > 1 \mu\text{g ml}^{-1}$) 31% and 52% of the mAbs elicited by XBB reinfection, respectively, but only 2% and 20% of the mAbs elicited by JN.1 reinfection. Compared with those elicited by XBB, JN.1-elicited A1 mAbs showed, on average, seven- to ten-fold higher neutralizing activity against JN.1, KP.2 and KP.3 (Fig. 4f and Extended Data Fig. 7a). Thus, in the context of WT-cross-reactive antibodies, JN.1 infection not only elicits higher neutralization against current JN.1-derived strains but also better enriches MBCs that encode effective class 1 or epitope group A1 antibodies. Nevertheless, JN.1-elicited WT-reactive A1 NAb exhibited 3.2-fold and 10-fold reductions in reactivities against KP.2 and KP.3, respectively. Only 24% retained their neutralization against KP.3 + A475V (Fig. 4f). This susceptibility raises concerns about the effectiveness of JN.1

boosters in counteracting ongoing viral evolution and indicates a need for vaccines derived from the KP.2/KP.3 lineage for robust protection against both current variants and future antigenic drifts.

The ‘broadly neutralizing’ A1 mAbs did not have significantly higher SHM rates or show significant preference in germline V(D) usage⁴⁵ (Extended Data Fig. 7b,c). The escaped A1 mAbs had higher DMS escape scores than the broadly neutralizing A1 mAbs on the mutations of interest, such as 456L and 475V on the basis of both antigens, but 455S and 493E only on the XBB.1.5 basis (Extended Data Fig. 7d,e). Previous structural analyses have indicated that IGHV3-53/3-66 mAbs primarily use their CDR-H1 and part of CDR-H3 to interact with RBD residue A475; however, we did not observe notable differences in CDR-H1 patterns^{10,43} (Extended Data Fig. 7f). Therefore, we propose that these A1 bnAbs rely on a distinctive core CDR-H3 and highly matured light chain for broad neutralization, as suggested by the preferences in *IGHD* gene usage (Extended Data Fig. 7g,h).

Recent growth advantages of JN.1 subvariants with mutations on the A1 epitope indicate the notable abundance of such NAb within the global population. This was also demonstrated by assessment of the average immune pressure by aggregating DMS profiles of WT-reactive mAbs from reinfection cohorts using a neutralization-weighted, codon-aware strategy, as described previously^{5,8}. Despite the accumulation of escape mutations on the A1 epitope and the verified significant evasion, the retained A1 bnAbs still exerted pressure on residues within

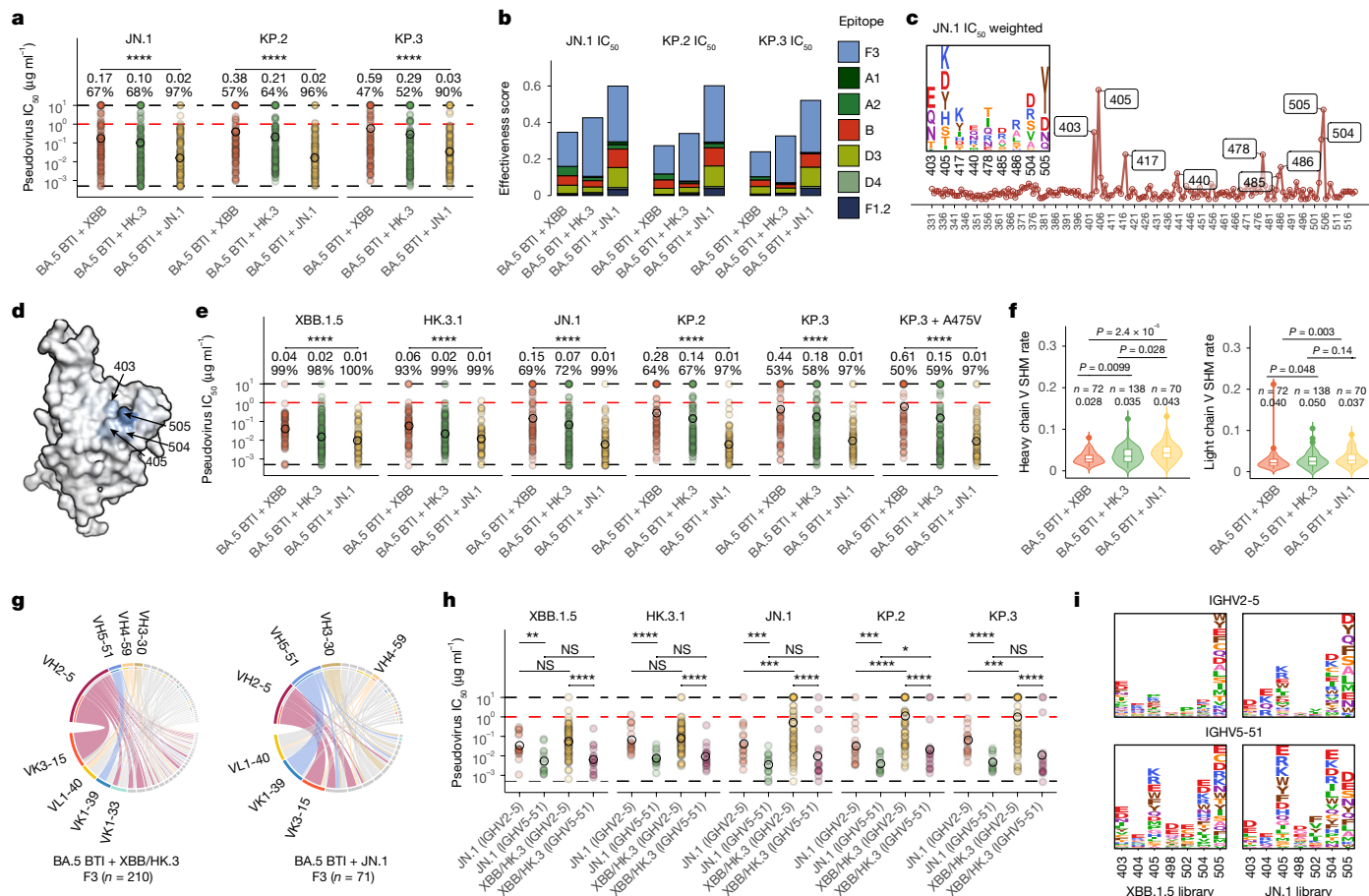


Fig. 5 | Broad neutralization of Omicron-specific NAbs. **a**, Neutralization activities of Omicron-specific mAbs isolated from three BTI + reinfection cohorts against JN.1, KP.2 and KP.3. Geometric mean IC_{50} values ($\mu\text{g ml}^{-1}$) and percentages of mAbs with $IC_{50} < 1 \mu\text{g ml}^{-1}$ are labelled above each group of points. **b**, Stacked bar charts showing the effectiveness scores of Omicron-specific mAbs for each epitope group weighted by IC_{50} against JN.1, KP.2 and KP.3. **c**, Calculation of immune pressure on each RBD site and mutation on the basis of the average of Omicron-specific antibody escape mutation profiles weighted by JN.1, and DMS for RBD expression and ACE2 binding. Hotspot residues are labelled and shown in logo plots. **d**, Average DMS site escape scores of mAbs in epitope group F3. Hotspot residues are indicated by arrows. **e**, Neutralization activities of

Omicron-specific mAbs in group F3 isolated from BTI + reinfection cohorts. Geometric mean IC_{50} values ($\mu\text{g ml}^{-1}$) and percentages of mAbs with $IC_{50} < 1 \mu\text{g ml}^{-1}$ (red dashed lines) are labelled above each group of points. Black dashed lines indicate limits of detection (0.005 and $10 \mu\text{g ml}^{-1}$). **f**, Comparison of SHM rates of F3 mAbs elicited by BA.5 BTI + XBB, HK.3 and JN.1 reinfection cohorts. **g**, Chord diagram showing the heavy–light chain V gene pairing of mAbs isolated from BA.5 BTI + XBB/HK.3 or JN.1 in epitope group F3. **h**, Neutralization activities of Omicron-specific mAbs in group F3 isolated from BA.5 BTI + XBB/HK.3 or JN.1 cohort encoded by IGHV2-5 or IGHV5-1. **i**, Average DMS escape mutation scores of F3 mAbs encoded by IGHV2-5 or IGHV5-1.

its epitope hotspots, including 403, 420, 455, 475 and 493 (Fig 4g–i). Unsurprisingly, the F456L mutation in KP.2 and KP.3 eliminated the L456 hotspot observed in JN.1 weighting; however, the score on residue E493 was even more pronounced in the KP.3 weighting, as this mutation enabled four new one-nucleotide-accessible amino acid mutations at this site, including Ala, Asp, Gly and Val.

In summary, among the WT-reactive NAbs, A1 remains the most pronounced epitope group against JN.1 subvariants, despite multiple evasive mutations on its epitope during recent viral evolution. Therefore, the development of boosters based on JN.1, or even JN.1 + F456L, KP.2 or KP.3, should be considered to better elicit bnAbs and enrich for effective MBCs that can resist potential future immune escape mutations, particularly in individuals receiving mRNA vaccines, whose immune responses predominantly elicit WT-reactive antibodies.

Potential of Omicron-specific NAbs

Unlike that caused by mRNA vaccination, immune imprinting caused by inactivated vaccines seems to be mitigated by Omicron reinfection, which elicits a substantial amount of Omicron-specific antibody. As

global vaccination strategies shift away from WT components and update to the latest variants, such mAbs may become the primary contributors to immune pressure in the future. Notably, JN.1 infection also induces Omicron-specific NAbs with significantly enhanced neutralization breadth against the JN.1 lineage compared with XBB or HK.3 infections (Fig. 5a). Epitope group F3 has the greatest neutralization breadth, with minor contributions from A2, B, D3 and F1.2 (Fig. 5b). A2 NAbs are likely to be evaded owing to their high epitope overlap with group A1. Notably, groups B and D3 include both WT-reactive and non-reactive bnAbs (Figs. 4b and 5b). BTI cohorts elicit more WT-reactive B/D3 mAbs than unvaccinated cohorts, and these cross-reactive B/D3 mAbs have a higher SHM rate than Omicron-specific ones (Extended Data Fig. 8a,b). Despite their cross-reactivity to WT, these antibodies demonstrate much higher neutralization activities against BA.5 compared with D614G, indicating potential Omicron-adaptive maturation (Extended Data Fig. 8c). WT-reactive and Omicron-specific B mAbs are derived from largely different heavy and light chain genes; however, D3 mAbs predominantly use IGHV5-1 regardless of their cross-reactivity (Extended Data Fig. 8d,e). Specific group B mAbs have higher DMS escape scores on residues 478 and 486, and D3 mAbs have higher scores

on residue 440; these residues are mutated sites in Omicron lineages (Extended Data Fig. 8f,g). Many Omicron-specific B NAbS (but not D3) do not neutralize BA.1 and BA.2, which do not harbour the F486V/S/P mutations found in post-BA.5 variants, owing to their vulnerability to 486 mutations (Extended Data Fig. 8h).

Despite the abundance of potent Omicron-specific NAbS in individuals who have experienced reinfection following previous inactivated vaccinations, we found minimal evidence of mutations that enable escape from these NAbS. The lack of escape mutations against such NAbS is particularly notable in China, where most of the population has received inactivated vaccines combined with BA.5/BF.7 BTI or even experienced more reinfections, suggesting weak selective pressure or inherent evolutionary constraints. Through aggregation of DMS profiles of Omicron-specific NAbS, we found that all escape hotspots except for G504 were located on residues of the RBD that have mutated in the Omicron variant (Fig. 5c). Given the potential for neutralization recovery of previously escaped NAbS, these mutated sites may have a reduced likelihood of further mutation. Notably, mutations at G504 have been recently reported to enhance serum neutralization, probably owing to their regulatory impact on the up–down dynamics of the spike glycoprotein⁴⁶. As anticipated, the four most prominent hotspots, encompassing residues 403, 405, 504 and 505, were all targeted by epitope F3 (Fig. 5d). In addition, NAbS induced by JN.1 showed notable breadth of neutralization against all tested JN.1 subvariants, outperforming those induced by XBB and HK.3 (Fig. 5e). This superiority is not surprising, as no further mutations have occurred on the escape hotspots of these NAbS following the R403K mutation in BA.2.86. Higher SHM rates were observed in HK.3 and JN.1-induced F3 mAbS than in those induced by XBB; this was inconsistent with the neutralization results, in which XBB and HK.3 exhibited similar neutralization capabilities. This discrepancy suggests that maturation is not the predominant factor determining the broad neutralization efficacy of F3 (Fig. 5f).

Instead, F3 mAbS showed intriguing patterns in the use of heavy and light chain V genes. F3 antibodies elicited by a single Omicron exposure, such as those in the XBB infection and XBB BTI cohorts, were almost exclusively derived from the IGHV2-5 and IGKV3-15 pairing (Extended Data Fig. 9a). However, these NAbS exhibited weak neutralization against JN.1 lineages (Extended Data Fig. 9b). By contrast, repeated Omicron infections diversified the germline utilization of F3 mAbS and generated F3 mAbS of comparable breadth regardless of vaccination (Fig. 5g and Extended Data Fig. 9c,d). Notably, JN.1 infection increased the use of IGHV5-51, particularly when paired with IGKV1-39. Regardless of the source cohort, IGHV5-51 F3 antibodies were significantly more effective against JN.1 lineages than IGHV2-5-derived ones (Fig. 5h). However, we did not observe lower DMS scores on residue 403, despite the presence of R403K in all BA.2.86 subvariants. Conversely, these IGHV5-51 F3 broad bnAbS had higher escape scores on residues 405 and 504 (Fig. 5i). IGHV5-51 seems to be a noteworthy germline heavy chain V gene in the context of the antigenicity and immunogenicity of the JN.1 lineage. Specifically, IGHV5-51 encompasses three main epitope groups, E3, D3 and F3, with distinct patterns of light chain usage. E3 and F3 favour IGLV1-44 and IGKV1-39, respectively, whereas IGHV5-51 D3 mAbS use a wide range of light chain V genes (Extended Data Fig. 9e). The SHM rates of these groups did not show significant differences, and their neutralization capabilities were closely aligned with the properties of their respective epitope groups (Extended Data Fig. 9f,g). These findings underscore the superior efficacy of JN.1-elicited Omicron-specific NAbS and the potency of these NAbS, especially the IGHV5-51-encoding F3 NAbS, against all Omicron variants; thus, they should be considered as potential targets for the development of vaccines.

Clash of class I and Omicron-specific NAbS

Recent research has demonstrated exceptionally strong immune imprinting in individuals vaccinated with mRNA vaccines, as these

individuals fail to mount an Omicron-specific antibody response even following several Omicron exposures^{6,7,31}. However, this phenomenon could not be observed in individuals who received inactivated vaccines, or in mRNA-vaccinated mice^{6,8}. Upon comprehensive characterization of Omicron-specific antibodies, we discovered that all Omicron-specific neutralizing epitopes on RBD competed with the A1 mAbS, which are well known for convergent use of the IGHV3-53/3-66 germline (Extended Data Fig. 10a,b). This competition was confirmed by SPR-based competition assays (Extended Data Fig. 10c). Given these results, we propose that the presence of the IGHV3-53/3-66 convergent response is pivotal in this robust imprinting^{47,48}.

In essence, inactivated vaccines induce a weaker convergent response compared with mRNA vaccines. The individuals studied in our research experienced the ‘zero COVID’ period in China during 2021–2022, leading to significant antibody waning. As a result, the concentration of Omicron-effective IGHV3-53/3-66 NAbS and corresponding MBCs may have been insufficient to effectively mask the antigen upon initial exposure to Omicron. This scenario would allow Omicron-specific naive B cells to be activated and promoted to mature. These activated B cells could then be recalled by subsequent Omicron exposure, leading to the generation of extensive Omicron-specific MBCs and antibodies. By contrast, the strong convergent responses in mRNA-vaccinated individuals may efficiently mask all Omicron-specific epitopes during the first Omicron encounter⁴⁹. In these individuals, MBCs encoding effective IGHV3-53/3-66 public antibodies would be repeatedly activated with each Omicron exposure, resulting in notable immune imprinting. Importantly, the ACE2-mimicking capability of these antibodies is also crucial, as it constrains viral evolution and ensures that the mAbS are not entirely evaded. Mice, which lack the IGHV3-53/3-66 germline, cannot generate a convergent response with large amounts of ACE2-mimicking NAbS, even if they receive mRNA vaccines. It is important to note that these analyses are preliminary and intuitive, and they require further rigorous experimental validation (Extended Data Fig. 10d).

Discussion

The ongoing evolution of JN.1 subvariants, particularly those with mutations on the A1 epitope—which are more likely to affect receptor-binding capabilities and potentially cause epistatic effects, akin to those seen in KP.3—necessitates vigilant monitoring. We emphasize the importance of V3-53/66 WT-reactive NAbS, which has also been highlighted in a concurrent study⁵⁰. We further point to the potential of F3 Omicron-specific NAbS elicited by Omicron reinfection cohorts in achieving broad neutralization against the JN.1 lineage.

Although infection with JN.1 elicits satisfactory cross-neutralization against its subvariants, supporting the efficacy of JN.1-based vaccine boosters, it is advisable to consider developing future vaccine boosters based on KP.2/KP.3 to enhance generation of effective bnAbS against future antigenic drifts. For individuals who have received mRNA vaccines, the induction of WT-cross-reactive bnAbS in epitope group A1 through these boosters is particularly crucial for achieving broad-spectrum protection against both current and emerging SARS-CoV-2 variants. In addition, if our hypothesis concerning the mechanism of heavy immune imprinting is correct, the use of a variant that demonstrates significant escape from A1 mAbS could mitigate the effects of immune imprinting and effectively elicit Omicron-specific NAbS.

Online content

Any methods, additional references, Nature Portfolio reporting summaries, source data, extended data, supplementary information, acknowledgements, peer review information; details of author contributions and competing interests; and statements of data and code availability are available at <https://doi.org/10.1038/s41586-024-08315-x>.

1. Yang, S. et al. Fast evolution of SARS-CoV-2 BA.2.86 to JN.1 under heavy immune pressure. *Lancet Infect. Dis.* **24**, e70–e72 (2023).
2. Huiberts, A. J. et al. Effectiveness of Omicron XBB.1.5 vaccine against infection with SARS-CoV-2 Omicron XBB and JN.1 variants, prospective cohort study, the Netherlands, October 2023 to January 2024. *Eurosurveillance* **29**, 2400109 (2024).
3. Kaku, Y. et al. Virological characteristics of the SARS-CoV-2 JN.1 variant. *Lancet Infect. Dis.* **24**, e82 (2024).
4. Cao, Y. et al. Omicron escapes the majority of existing SARS-CoV-2 neutralizing antibodies. *Nature* **602**, 657–663 (2022).
5. Cao, Y. et al. Imprinted SARS-CoV-2 humoral immunity induces convergent Omicron RBD evolution. *Nature* **614**, 521–529 (2023).
6. Liang, C.-Y. et al. Imprinting of serum neutralizing antibodies by Wuhan-1 mRNA vaccines. *Nature* **630**, 950–960 (2024).
7. Tortorici, M. A. et al. Persistent immune imprinting occurs after vaccination with the COVID-19 XBB.1.5 mRNA booster in humans. *Immunity* **57**, 904–911.e4 (2024).
8. Yisimayi, A. et al. Repeated Omicron exposures override ancestral SARS-CoV-2 immune imprinting. *Nature* **625**, 148–156 (2024).
9. Yang, S. et al. Antigenicity and infectivity characterisation of SARS-CoV-2 BA.2.86. *Lancet Infect. Dis.* **23**, e457–e459 (2023).
10. Liu, C. et al. A structure-function analysis shows SARS-CoV-2 BA.2.86 balances antibody escape and ACE2 affinity. *Cell Rep. Med.* **5**, 101553 (2024).
11. Yue, C. et al. ACE2 binding and antibody evasion in enhanced transmissibility of XBB.1.5. *Lancet Infect. Dis.* **23**, 278–280 (2023).
12. Jian, F. et al. Convergent evolution of SARS-CoV-2 XBB lineages on receptor-binding domain 455–456 synergistically enhances antibody evasion and ACE2 binding. *PLoS Pathog.* **19**, e1011868 (2023).
13. Jian, F. et al. Further humoral immunity evasion of emerging SARS-CoV-2 BA.4 and BA.5 subvariants. *Lancet Infect. Dis.* **22**, 1535–1537 (2022).
14. Starr, T. N. et al. Deep mutational scans for ACE2 binding, RBD expression, and antibody escape in the SARS-CoV-2 Omicron BA.1 and BA.2 receptor-binding domains. *PLoS Pathog.* **18**, e1010951 (2022).
15. Taylor, A. L. & Starr, T. N. Deep mutational scans of XBB.1.5 and BQ.1.1 reveal ongoing epistatic drift during SARS-CoV-2 evolution. *PLoS Pathog.* **19**, e1011901 (2023).
16. Wang, Q. et al. XBB.1.5 monovalent mRNA vaccine booster elicits robust neutralizing antibodies against XBB subvariants and JN.1. *Cell Host Microbe* **32**, 315–321.e3 (2024).
17. Jain, S. et al. XBB.1.5 monovalent booster improves antibody binding and neutralization against emerging SARS-CoV-2 Omicron variants. Preprint at *bioRxiv* <https://doi.org/10.1101/2024.02.03.578771> (2024).
18. Planas, D. et al. Distinct evolution of SARS-CoV-2 Omicron XBB and BA.2.86/JN.1 lineages combining increased fitness and antibody evasion. *Nat. Commun.* **15**, 2254 (2024).
19. Carabelli, A. M. et al. SARS-CoV-2 variant biology: immune escape, transmission and fitness. *Nat. Rev. Microbiol.* **21**, 162–177 (2023).
20. Ma, W., Fu, H., Jian, F., Cao, Y. & Li, M. Immune evasion and ACE2 binding affinity contribute to SARS-CoV-2 evolution. *Nat. Ecol. Evol.* **7**, 1457–1466 (2023).
21. Witte, L. et al. Epistasis lowers the genetic barrier to SARS-CoV-2 neutralizing antibody escape. *Nat. Commun.* **14**, 302 (2023).
22. Peng, R., Wu, L.-A., Wang, Q., Qi, J. & Gao, G. F. Cell entry by SARS-CoV-2. *Trends Biochem. Sci.* **46**, 848–860 (2021).
23. Li, L. et al. Spike structures, receptor binding, and immune escape of recently circulating SARS-CoV-2 Omicron BA.2.86, JN.1, EG.5, EG.5.1, and HV.1 sub-variants. *Structure* **32**, 1055–1067.e6 (2024).
24. Starr, T. N. et al. Shifting mutational constraints in the SARS-CoV-2 receptor-binding domain during viral evolution. *Science* **377**, 420–424 (2022).
25. Taylor, A. L. & Starr, T. N. Deep mutational scanning of SARS-CoV-2 Omicron BA.2.86 and epistatic emergence of the KP.3 variant. *Virus Evol.* **10**, veae067 (2024).
26. Simon-Loriere, E. & Schwartz, O. Towards SARS-CoV-2 serotypes? *Nat. Rev. Microbiol.* **20**, 187–188 (2022).
27. Du, P. et al. The omicron BA.2.86 subvariant as a new serotype of SARS-CoV-2. *Lancet Microbe* **5**, e516 (2024).
28. Cao, Y. et al. Characterization of the enhanced infectivity and antibody evasion of Omicron BA.2.75. *Cell Host Microbe* **30**, 1527–1539.e5 (2022).
29. Cao, Y. et al. BA.2.12.1, BA.4 and BA.5 escape antibodies elicited by Omicron infection. *Nature* **608**, 593–602 (2022).
30. Cao, Y. et al. Potent neutralizing antibodies against SARS-CoV-2 identified by high-throughput single-cell sequencing of convalescent patients' B cells. *Cell* **182**, 73–84.e16 (2020).
31. Addetia, A. et al. Neutralization, effector function and immune imprinting of Omicron variants. *Nature* **621**, 592–601 (2023).
32. Robbiani, D. F. et al. Convergent antibody responses to SARS-CoV-2 in convalescent individuals. *Nature* **584**, 437–442 (2020).
33. Starr, T. N. et al. Deep mutational scanning of SARS-CoV-2 receptor binding domain reveals constraints on folding and ACE2 binding. *Cell* **182**, 1295–1310.e20 (2020).
34. Cao, Y. et al. Humoral immune response to circulating SARS-CoV-2 variants elicited by inactivated and RBD-subunit vaccines. *Cell Res.* **31**, 732–741 (2021).
35. Cao, Y. et al. Humoral immunogenicity and reactogenicity of CoronaVac or ZF2001 booster after two doses of inactivated vaccine. *Cell Res.* **32**, 107–109 (2022).
36. Barnes, C. O. et al. SARS-CoV-2 neutralizing antibody structures inform therapeutic strategies. *Nature* **588**, 682–687 (2020).
37. Loo, Y. M. et al. The SARS-CoV-2 monoclonal antibody combination, AZD7442, is protective in nonhuman primates and has an extended half-life in humans. *Sci. Transl. Med.* **14**, eabl8124 (2022).
38. Copin, R. et al. The monoclonal antibody combination REGEN-COV protects against SARS-CoV-2 mutational escape in preclinical and human studies. *Cell* **184**, 3949–3961.e11 (2021).
39. Westendorf, K. et al. LY-CoV1404 (bebtelovimab) potentially neutralizes SARS-CoV-2 variants. *Cell Rep.* **39**, 110812 (2022).
40. Cao, Y. et al. Rational identification of potent and broad sarbecovirus-neutralizing antibody cocktails from SARS convalescents. *Cell Rep.* **41**, 111845 (2022).
41. Rappazzo, C. G. et al. Broad and potent activity against SARS-like viruses by an engineered human monoclonal antibody. *Science* **371**, 823–829 (2021).
42. Starr, T. N. et al. SARS-CoV-2 RBD antibodies that maximize breadth and resistance to escape. *Nature* **597**, 97–102 (2021).
43. Yuan, M. et al. Structural basis of a shared antibody response to SARS-CoV-2. *Science* **369**, 1119–1123 (2020).
44. Zhang, Q. et al. Potent and protective IGHV3-53/3-66 public antibodies and their shared escape mutant on the spike of SARS-CoV-2. *Nat. Commun.* **12**, 4210 (2021).
45. Li, L. et al. Breakthrough infection elicits hypermutated IGHV3-53/3-66 public antibodies with broad and potent neutralizing activity against SARS-CoV-2 variants including the emerging EG.5 lineages. *PLoS Pathog.* **19**, e1011856 (2023).
46. Dadonaite, B. et al. Spike deep mutational scanning helps predict success of SARS-CoV-2 clades. *Nature* **631**, 617–626 (2024).
47. Schaefer-Babajew, D. et al. Antibody feedback regulates immune memory after SARS-CoV-2 mRNA vaccination. *Nature* **613**, 735–742 (2023).
48. Bergström, J. J. E., Xu, H. & Heyman, B. Epitope-specific suppression of IgG responses by passively administered specific IgG: evidence of epitope masking. *Front. Immunol.* **8**, 238 (2017).
49. Wang, Z. et al. mRNA vaccine-elicited antibodies to SARS-CoV-2 and circulating variants. *Nature* **592**, 616–622 (2021).
50. Paciello, I. et al. B cell maturation restored ancestral germlines to control Omicron BA.2.86. Preprint at *bioRxiv* <https://doi.org/10.1101/2024.03.03.583187> (2024).

Publisher's note Springer Nature remains neutral with regard to jurisdictional claims in published maps and institutional affiliations.



Open Access This article is licensed under a Creative Commons Attribution-NonCommercial-NoDerivatives 4.0 International License, which permits any non-commercial use, sharing, distribution and reproduction in any medium or format, as long as you give appropriate credit to the original author(s) and the source, provide a link to the Creative Commons licence, and indicate if you modified the licensed material. You do not have permission under this licence to share adapted material derived from this article or parts of it. The images or other third party material in this article are included in the article's Creative Commons licence, unless indicated otherwise in a credit line to the material. If material is not included in the article's Creative Commons licence and your intended use is not permitted by statutory regulation or exceeds the permitted use, you will need to obtain permission directly from the copyright holder. To view a copy of this licence, visit <http://creativecommons.org/licenses/by-nc-nd/4.0/>.

© The Author(s) 2024

Methods

Plasma isolation

Blood samples were collected from individuals who had either recovered from or been reinfected with the SARS-CoV-2 Omicron BTI variant. This was done under the research protocol approved by the Beijing Ditan Hospital, affiliated with Capital Medical University (Ethics Committee Archiving No. LL-2021-024-02), the Tianjin Municipal Health Commission and the Ethics Committee of Tianjin First Central Hospital (Ethics Committee Archiving No. 2022N045KY). All participants provided their agreement for the collection, storage and use of their blood samples strictly for research purposes and the subsequent publication of related data. SARS-CoV-2 infections were confirmed by either antigen or PCR tests. Specific strains of infection were inferred on the basis of the sampling time when the corresponding strain accounted for most of the detected sequences in the region of sample collection. The interval between last exposure and sampling was 33 ± 8.9 days (mean \pm s.d.).

Patients in the reinfection group were initially infected with the BA.5/BF.7 variants in December 2022 in Beijing and Tianjin, China⁵¹. From 1 December 2022 to 1 February 2023, more than 98% of the sequenced samples were identified as BA.5* (excluding BQ*), primarily consisting of the subtypes BA.5.2.48* and BF.7.14*, which were representative of the BA.5/BF.7 variants during this period. Subsequently, patients in the XBB BTI cohort and those with secondary infections in the reinfection group contracted the virus between May and June 2023. More than 90% of the sequenced samples from Beijing and Tianjin during this period corresponded to the XBB*+486P variant. Plasma samples were isolated and tested for neutralization titres against SARS-CoV-2 variant spike-pseudotyped vesicular stomatitis virus (VSV). Whole blood was diluted in a 1:1 ratio with a solution of PBS supplemented with 2% fetal bovine serum. This was followed by Ficoll gradient centrifugation (Cytiva, 17-1440-03). After centrifugation, the plasma was collected from the upper layer, stored in aliquots at 20 °C or lower and heat-inactivated before use in experiments.

Pseudovirus preparation and neutralization

The SARS-CoV-2 variant spike protein pseudovirus was generated using the VSV pseudovirus packaging system as described previously^{8,52}. In addition to previously constructed variants, we included 'FLiRT'/KP.2 (JN.1 + R346T + F456L), KP.3 (JN.1 + F456L + Q493E) and their subvariants with S31del (SARS-CoV-2 ancestral strain numbering). The spike protein gene was codon-optimized and integrated into the pcDNA3.1 expression plasmid using the BamHI and XbaI restriction enzyme sites to augment the expression efficiency of the spike protein in mammalian cells. During pseudovirus production, the 293T cells (American Type Culture Collection, CRL-3216) were transfected with the SARS-CoV-2 spike protein expression plasmid. After transfection, these cells were infected with the G* Δ G-VSV virus (VSV-G pseudotyped virus, Kerafast) present in the cell culture supernatant. The pseudovirus was subsequently harvested and filtered from the supernatant aliquoted, and stored at -80 °C for later use.

Pseudovirus neutralization assays were performed using the Huh-7 cell line (Japan Collection of Research Bioresources, 0403). Plasma samples were serially diluted and mixed with the pseudovirus. After an incubation period of 1 h at 37 °C with 5% CO₂, digested Huh-7 cells were introduced, followed by incubation for a further 24 h at 37 °C. The supernatant was then removed, and the mixture was incubated with D-luciferin reagent (PerkinElmer, 6066769) in darkness for 2 min. The cell lysate was transferred to a detection plate, and the luminescence intensity was measured using a microplate spectrophotometer (PerkinElmer, HH3400). NT₅₀ values were determined using a four-parameter logistic regression model⁵³.

Surface plasmon resonance

SPR experiments were conducted on a Biacore 8K (Cytiva) to determine the RBD-hACE2 binding affinities. hACE2-Fc was immobilized

on to Protein A sensor chips (Cytiva). Purified SARS-CoV-2 variant RBD samples prepared in serial dilutions (6.25, 12.5, 25, 50 and 100 nM) were injected on the sensor chips. Response units were recorded using Biacore 8K Evaluation Software 3.0 (Cytiva) at room temperature. Raw response data were fitted to 1:1 binding models to determine the association and dissociation kinetic constants (k_a and k_d) and binding affinities (dissociation equilibrium constant K_D) using Biacore 8K Evaluation Software v.3.0 (Cytiva).

In the competitive binding assays, we used anti-His-tagged CMS sensor chips (Cytiva) to immobilize 5 μ g ml⁻¹ of the RBD protein for a duration of 1 min. Subsequently, a concentration of 20 μ g ml⁻¹ of antibody 1 was introduced for 2 min, followed by the introduction of antibody 2 at an identical concentration and for the same duration. We used Glycine 1.5 for the regeneration phase.

mRNA vaccine preparation and mouse immunization

For mRNA vaccine preparation, the 5' untranslated region, target sequence and 3' untranslated region were sequentially integrated downstream of the T7 promoter in an empty PSP73 plasmid. Subsequently, a double-digestion process was used to produce linearized DNA. This DNA served as a template for a T7 RNA polymerase-driven in vitro transcription process to generate RNA that encoded the SARS-CoV-2 S6P (F817P, A892P, A899P, A942P, K986P, V987P, R683A and R685A) protein, according to the manufacturer's instructions (Vazyme, DD4201). The transcriptional outputs were subjected to DNase I treatment for elimination of DNA templates, followed by a purification step using VAHTS RNA Clean Beads (Vazyme, N412-02). The cap 1 structure was added using Vaccinia Capping Enzyme (Vazyme, DD4109) and mRNA cap 2'-O-methyltransferase (Vazyme, DD4110), with a subsequent purification using magnetic beads. Poly(A) tails were incorporated using *Escherichia coli* Poly(A) Polymerase (Vazyme, N4111-02), followed by another round of purification.

The mRNA was encapsulated in a functionalized lipid nanoparticle as described previously⁵⁴. Concisely, a solution containing ionizable lipid, DSPC, cholesterol and PEG2000-DMG was prepared in ethanol, with a molar ratio of 50:10:38.5:1.5. The mRNA was then diluted in a 50 mM citrate buffer (pH 4.0), free of RNase, to achieve a final lipid/mRNA weight ratio of 6:1. The aqueous and ethanol solutions were mixed in a 3:1 volume ratio using a microfluidic apparatus, and the obtained lipid nanoparticles were then subjected to overnight dialysis. To preserve the chemical stability of the components, all samples were stored at temperatures ranging from 2 to 8 °C for up to a week. The dimensions and distribution of particle sizes of the lipid nanoparticles were assessed, as were the encapsulation efficiency and concentration of mRNA; the encapsulation rates were found to be typically between 90% and 99%.

Animal experiments were carried out under study protocols approved by the Rodent Experimental Animal Management Committee of the Institute of Biophysics, Chinese Academy of Sciences (SYXK2023300), and the Animal Welfare Ethics Committee of HFK Biologics (HFK-AP-20210930). Ten female BALB/c mice, aged between 6 and 8 weeks, were used in each group. The number of animals was determined on the basis that differences between experimental groups could be confirmed. No randomization or blinding was performed. The mice were housed under a 12 h light, 12 h dark cycle, with room temperatures maintained between 20 °C and 26 °C and humidity levels between 30% and 70%. mRNA vaccines were given intramuscularly at a dosage of 10 μ g per mouse. Blood samples were collected 2 weeks after the final immunization, as shown in Extended Data Fig. 3a.

Antigen-specific cell sorting and single-cell V(D)J sequencing

PBMCs and plasma were isolated from blood samples using Ficoll (Cytiva, 17-1440-03) density gradient centrifugation. B cells were enriched from PBMCs using a CD19⁺ positive selection kit (STEM-CELL, 17854). The enriched B cells were then stained with the RBD of the last infected variant, as well as the RBD of the ancestral strain. B cells

were also stained with antibodies against CD20 (BioLegend, 302304), CD27 (BioLegend, 302824), IgM (BioLegend, 314532), IgD (BioLegend, 348210) and 7-AAD (Invitrogen, 00-6993-50).

B cells that were positive for the RBD of the last infected variant (XBB.1.5, HK.3 or JN.1), CD20 and CD27, but negative for IgM, IgD and 7-AAD, were sorted. These RBD-binding B cells were subsequently subjected to single-cell V(D)J sequencing using a Chromium Next GEM Single Cell V(D)J Reagent Kit (v.1.1) according to the manufacturer's user guide (10x Genomics, CG000208). The 10x Genomics V(D)J Illumina sequencing data were assembled as B cell receptor contigs and aligned to the GRCh38 B cell receptor reference using the Cell Ranger (v.6.1.1) pipeline. For quality control, only the productive contigs and B cells with one heavy chain and one light chain were kept. The germline V(D)J genes were identified and annotated using IgBlast (v1.17.1)⁵⁵. SHM nucleotides and residues in the antibody variable domain were detected using Change-O toolkit (v.1.2.0)⁵⁶.

Expression and purification of mAbs

Antibody heavy and light chain genes were first optimized for human cell expression and synthesized by GenScript. VH and VL segments were separately inserted into plasmids (pCMV3-CH, pCMV3-CL or pCMV3-CK) through infusion (Vazyme, C112). Plasmids encoding heavy chains and light chains of antibodies were cotransfected into DH5 α chemically competent cells (Tsingke, TSC-C01-96) and spread on to LB solid medium (Beyotime, ST158) supplemented with ampicillin (Solarbio, A1170), and single colonies cultured overnight were selected for PCR identification. Positive bacterial cultures were subjected to Sanger sequencing for verification. Finally, positive clones were selected on the basis of sequence alignment, expanded for culture, and subjected to plasmid extraction (CWBIO CW2105).

Expi-293F cells with a density of $0.30\text{--}0.35 \times 10^6$ cells ml^{-1} were subcultured in 20 ml of culture medium (OPM Biosciences, 81075-001), sealed and incubated at 37°C , 125 ± 5 rpm in an 8% CO_2 atmosphere. When the cell density reached $2\text{--}3 \times 10^6$ cells ml^{-1} (typically in 3 days), the cells were treated with medium to dilute the density to 2×10^6 cells ml^{-1} and cultured overnight. For transfection, the antibody-encoding plasmids were diluted with 0.9% NaCl solution, mixed with polyethylenimine transfection reagent (Yeasen, 40816ES03) and added to the cell culture. The reaction bottle was then returned to the shaker and incubated at 37°C , 8% CO_2 and 125 ± 5 rpm. Twenty-four hours after transfection, the matching feed solution (OPM Biosciences, F081918-001) (1 ml per bottle) was added, and feeding was performed every other day for 6–10 days.

For antibody purification, the expression culture was centrifuged at 3,000g for 10 min to remove cells, and the supernatant was collected. Protein A Magnetic beads (GenScript, L00695) were added, followed by incubation at room temperature for 2 h; then, the beads were transferred to a 24-well plate and purified using a KingFisher automated system (Thermo Fisher). The purified antibody protein was quantified using a Nanodrop (Thermo Fisher, 840-317400), and the purity was confirmed by SDS-PAGE (LabLead, P42015).

Enzyme-linked immunosorbent assays

SARS-CoV-2 XBB.1.5, HK.3 and JN.1 RBD were individually aliquoted into a 96-well plate, which was then incubated overnight at 4°C . The plate was then washed three times with PBST (PBS with Tween-20). Subsequently, the wells were blocked with 3–5% bovine serum albumin in PBST at 37°C for 2 h. After another three washes with PBST, $100 \mu\text{l}$ of $1 \mu\text{g ml}^{-1}$ antibodies were added to each well, followed by incubation for 30 min at room temperature. The plate was washed five times to remove unbound antibodies. Peroxidase-conjugated AffiniPure Goat Anti-Human IgG(H+L) (JACKSON, 109-035-003) was added, followed by incubation at room temperature for 15 min, then five washes with PBST. The substrate tetramethylbenzidine (Solarbio, 54827-17-7) was added, followed by incubation for a further 10 min. The enzymatic

reaction was halted by addition of 2 M H_2SO_4 . Finally, the absorbance of each well was measured at 450 nm using a microplate reader (Perkin-Elmer, HH3400).

Construction of DMS libraries

Replicate DMS libraries spanning from N331 to T531 (Wuhan-Hu-1 reference numbering) of SARS-CoV-2 XBB.1.5 and JN.1 variants were constructed as outlined previously^{1,2}. Initially, site-directed mutagenesis PCR with computationally designed NNS primers was conducted to generate all potential amino acid mutations on XBB.1.5 and JN.1 RBD. Then, each RBD variant was tagged with a unique 26-nucleotide (N26) barcode by PCR and assembled into a yeast surface display vector (Addgene, 166782). The XBB.1.5 and JN.1 DMS libraries were further transfected into electrocompetent DH10B cells for plasmid amplification and subjected to PacBio sequencing library preparation to determine the association between RBD variants and corresponding N26 barcodes. These enlarged DMS libraries were introduced into the EBY100 strain of *Saccharomyces cerevisiae*, screened on SD-CAA agar plates and subsequently expanded in SD-CAA liquid media; these were then flash-frozen in liquid nitrogen and preserved at -80°C .

Profiling of mutation effects on RBD expression

RBD expression profiling for JN.1 DMS libraries was performed as previously described². In brief, yeast libraries were recovered and propagated overnight at 30°C in SD-CAA from an original optical density at 600 nm (OD_{600}) of 0.1. RBD surface expression was induced by diluting the yeast cells back to SG-CAA at an initial OD_{600} of 0.67 and incubating the yeasts at room temperature with mild shaking for 16 h. Then, 45 OD units of induced yeasts were washed twice using PBSA (PBS supplemented with 0.2 mg l^{-1} bovine serum albumin, pH 7.4) and incubated with 1:100 diluted FITC-conjugated anti-c-MYC antibody (Immunology Consultants Lab, CMYC-45F) for 1 h at room temperature under gentle agitation. After washing with PBSA, these yeast cells were resuspended in PBSA for FACS. The above prepared yeasts were analysed with a BD FACS Aria III cytometer by gating for single events and further partitioning into four bins according to FITC fluorescence intensity: bin 1 captured 99% of non-labelled cells, whereas the remaining yeasts were equally divided among bins 2 to 4. In total, more than 25 million yeasts were collected across these four bins for each library. After sorting, yeasts from each collection tube were centrifuged for 5 min and resuspended in 5 ml SD-CAA. To quantify the yeast recovery rate after sorting, $10 \mu\text{l}$ of the postsorting sample from each bin was further diluted and spread on YPD agar plates; the remaining samples were grown overnight and subjected to plasmid extraction, N26 barcode amplification and next-generation sequencing.

MACS-based antibody mutation escape profiling

High-throughput mutation escape profiling for each mAb was conducted using magnetic-activated cell sorting (MACS) following a previously reported method¹. In brief, improperly folded RBD variants in XBB.1.5 and JN.1 DMS libraries were removed using ACE2 (Sino Biological, 10108-H08H-B) conjugated biotin binder beads (Thermo Fisher, 11533D). After being washed with PBSA, the beads that had captured RBD-expressing yeasts were released and enlarged in SD-CAA and then preserved as frozen aliquots at -80°C .

For MACS-based mutation escape profiling, the ACE2-binder yeasts were thawed in SD-CAA with shaking overnight and back-diluted into SG-CAA for RBD surface expression induction. Two sequential rounds of negative selection with any given antibody were used to eliminate specific antibody binders in libraries. Then, MYC-tag-based positive selection was performed using anti-c-Myc magnetic beads (Thermo Fisher Scientific, 88843) to capture the RBD-expressing yeasts in the antibody-escaping population after two rounds of negative selection.

The final yeast population was washed and grown overnight in SD-CAA and submitted to plasmid extraction with a 96-well yeast

plasmid extraction kit (Coolaber, PE053). N26 barcode amplification was conducted using the obtained plasmid as the PCR template; then, the amplified barcodes were further purified with 1× Ampure XP beads (Beckman Coulter, A63882) and subjected to single-end sequencing.

Antibody DMS data analysis

The raw sequencing data from the DMS were processed as previously described^{8,12}. Specifically, the barcode sequences detected from both the antibody-screened and reference libraries were aligned with a barcode-variant dictionary derived from PacBio sequencing data of the XBB.1.5 and JN.1 DMS libraries using the alignparse (v.0.6.2) and dms_variants (v.1.4.3) tools. Ambiguous barcodes were excluded during the merging of yeast libraries. Only barcodes detected more than five times in the reference library were considered for further analysis. The escape score for a variant X, present in both the screened and reference libraries, was calculated as $F \times (n_{X,ab}/N_{ab}) / (n_{X,ref}/N_{ref})$, where F is a scaling factor to normalize the scores to a 0–1 range, and n and N represent the numbers of detected barcodes for variant X and the total barcodes in the antibody-screened (ab) or reference (ref) samples, respectively. For antibodies subjected to DMS with multiple replicates using different mutant libraries, the final escape score for each mutation was averaged for subsequent analyses.

We used graph-based unsupervised clustering and embedding to assign an epitope group to each antibody and visualize them in a two-dimensional space. Initially, site escape scores (sum of mutation escape scores per residue) for each antibody were normalized to a sum of one, representing a distribution over RBD residues. The dissimilarity between two antibodies was quantified by the square root of the Jensen–Shannon divergence of the normalized escape scores. Pairwise dissimilarities for all antibodies in the dataset were computed using the SciPy module (scipy.spatial.distance.jensenshannon, v.1.7.0). A k -nearest-neighbour graph was constructed using the python-igraph module (v.0.9.6), and Leiden clustering was applied to assign a cluster to each antibody⁵⁷. Cluster names were manually annotated on the basis of the characteristic sites in the average escape profiles of each cluster, using the same nomenclature as our previously published DMS dataset⁸. To visualize the dataset in two dimensions, uniform manifold approximation and projection was performed on the basis of the k -nearest-neighbour graph using umap-learn module (v.0.5.2), and figures were generated using R package ggplot2 (v.3.3.3).

To compute the average immune pressure or identify escape hotspots using a collection of mAb DMS profiles, we followed a similar approach to that used in our previous study, incorporating four types of weight to account for the impact of each mutation on hACE2-binding affinity, RBD expression, neutralizing activity and codon constraints at each residue. Owing to the absence of ACE2-binding DMS data on the JN.1 basis, we used XBB.1.5-based results in our calculations to filter out ACE2-dampening mutations, which may introduce artifacts when strong epistasis is present^{5,8}. For codon usage constraints, mutations inaccessible through single nucleotide changes were assigned a weight of zero, whereas others received a weight of 1.0. We used JN.1 (EPI_ISL_18373905), KP.2 (EPI_ISL_18916251) and KP.3 (EPI_ISL_19036766) to define one-nucleotide-accessible amino acid mutations. Neutralizing activity weights were calculated as $-\log_{10}(IC_{50})$, with IC_{50} values below 0.0005 or above 1.0 adjusted to 0.0005 or 1.0, respectively. Raw escape scores for each antibody were normalized by the maximum score across all mutants. The weighted score for each antibody and mutation was

obtained by multiplying the normalized scores by the corresponding four weights, and the final mutation-specific weighted score was the sum of scores for all antibodies in the designated set, subsequently normalized to a 0–1 range. To visualize the calculated escape maps, sequence logos were generated using the Python module logomaker (v.0.8).

Reporting summary

Further information on research design is available in the Nature Portfolio Reporting Summary linked to this article.

Data availability

Information about mAbs involved in this study is included in the supplementary tables. Raw and processed DMS data and other necessary data related to this study are available at Zenodo (<https://doi.org/10.5281/zenodo.13893217>)⁵⁸.

Code availability

Custom scripts for reproduction of the analyses in this study are available at Zenodo (<https://doi.org/10.5281/zenodo.13893217>)⁵⁸ and GitHub (<https://github.com/yunlongcaolab/SARS-CoV-2-JN.1-mAbs>).

- Pan, Y. et al. Characterisation of SARS-CoV-2 variants in Beijing during 2022: an epidemiological and phylogenetic analysis. *Lancet* **401**, 664–672 (2023).
- Li, H. et al. Establishment of replication-competent vesicular stomatitis virus-based recombinant viruses suitable for SARS-CoV-2 entry and neutralization assays. *Emerg. Microbes Infect.* **9**, 2269–2277 (2020).
- Nie, J. et al. Establishment and validation of a pseudovirus neutralization assay for SARS-CoV-2. *Emerg. Microbes Infect.* **9**, 680–686 (2020).
- Yanez Arteta, M. et al. Successful reprogramming of cellular protein production through mRNA delivered by functionalized lipid nanoparticles. *Proc. Natl Acad. Sci. USA* **115**, E3351–E3360 (2018).
- Ye, J., Ma, N., Madden, T. L. & Ostell, J. M. IgBLAST: an immunoglobulin variable domain sequence analysis tool. *Nucleic Acids Res.* **41**, W34–W40 (2013).
- Gupta, N. T. et al. Change-O: a toolkit for analyzing large-scale B cell immunoglobulin repertoire sequencing data. *Bioinformatics* **31**, 3356–3358 (2015).
- Traag, V. A., Waltman, L. & van Eck, N. J. From Louvain to Leiden: guaranteeing well-connected communities. *Sci. Rep.* **9**, 5233 (2019).
- Jian, F., & Cao, Y. Resources of “Evolving antibody response to SARS-CoV-2 antigenic shift from XBB to JN.1”. *Zenodo* <https://doi.org/10.5281/zenodo.13893217> (2024).

Acknowledgements We thank all volunteers who provided blood samples. This study was financially supported by the Ministry of Science and Technology of China (grant no. 2023YFC3043200), Changping Laboratory (grant nos. 2021A0201 and 2021D0102) and the National Natural Science Foundation of China (grant nos. 32222030 and 2023011477).

Author contributions Y.C. designed and supervised the study. F.J. and Y.C. wrote the manuscript with input from all authors. A.Y., W.S., R.A., Yao Wang and X.N. performed B cell sorting, single-cell V(D)J sequencing experiments and data analysis. J.W. (BIOPIIC), H.S. and F.J. obtained and analysed the DMS data. J.W. (Changping Laboratory) and F.S. performed antibody expression and management. M.M. and W.W. constructed mRNA vaccines and conducted mouse immunization. Y.Y. and Youchun Wang constructed the pseudotyped virus. P.W., L.Y., T.X. and W.W. performed the pseudovirus neutralization assays, ELISAs and SPR experiments. Q.G. proofread the manuscript. Y.X., X.C., Z.S. and R.J. recruited the patients.

Competing interests Y.C. is listed as an inventor of provisional patent applications of SARS-CoV-2 RBD-specific antibodies. Y.C. is a cofounder of Singlomics Biopharmaceuticals. The remaining authors declare no competing interests.

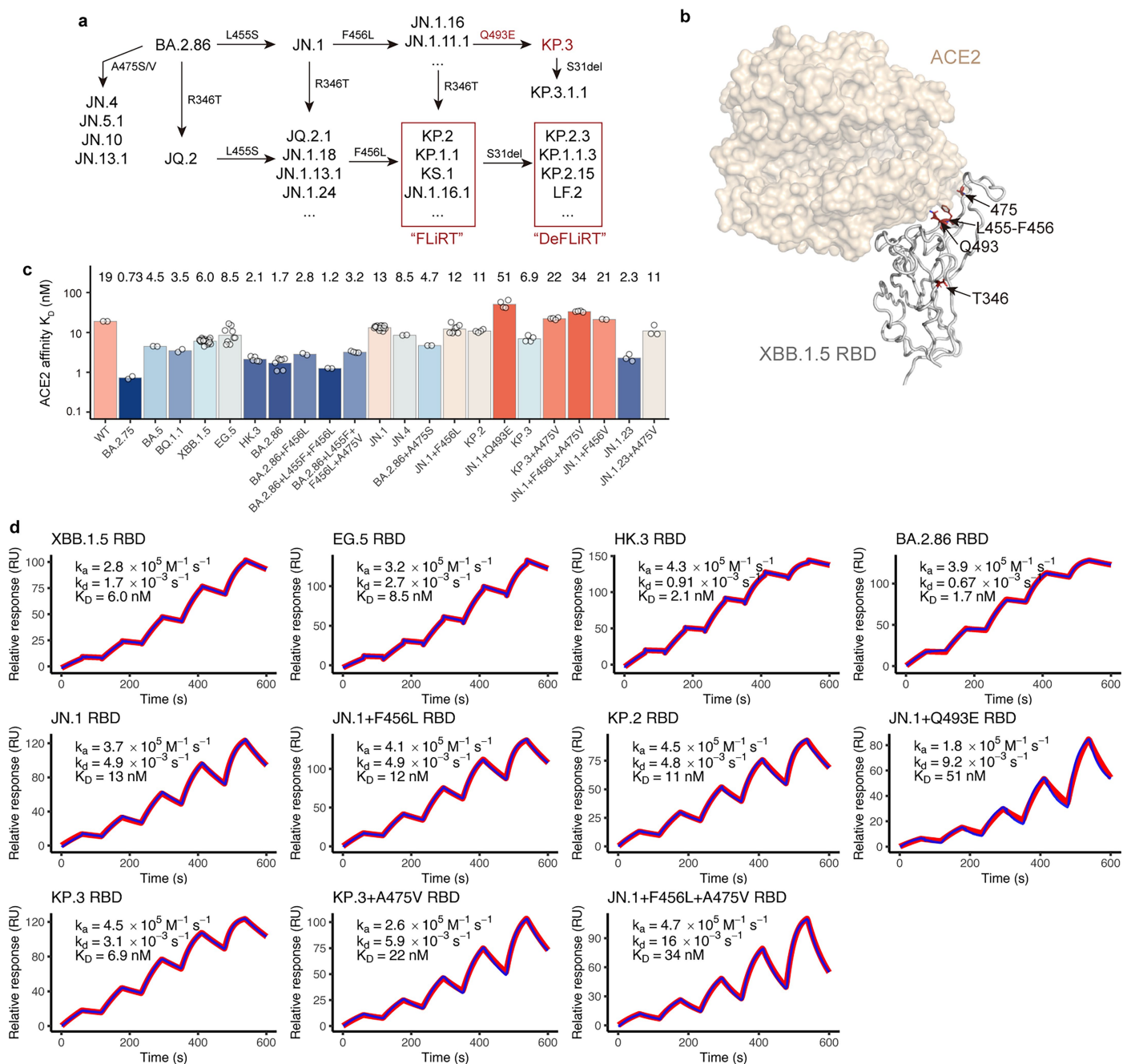
Additional information

Supplementary information The online version contains supplementary material available at <https://doi.org/10.1038/s41586-024-08315-x>.

Correspondence and requests for materials should be addressed to Yunlong Cao.

Peer review information Nature thanks Paul Moss and the other, anonymous, reviewer(s) for their contribution to the peer review of this work. Peer reviewer reports are available.

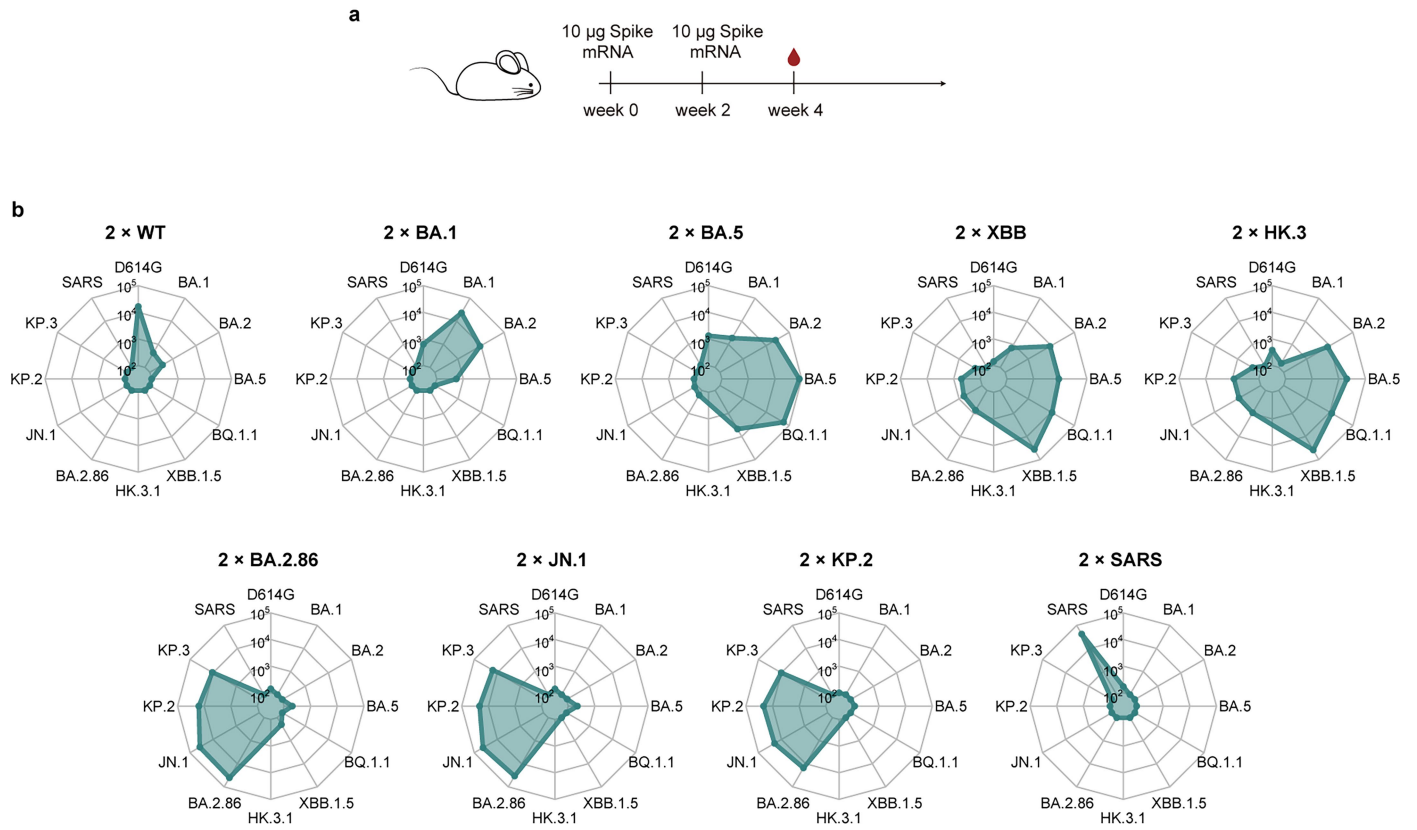
Reprints and permissions information is available at <http://www.nature.com/reprints>.



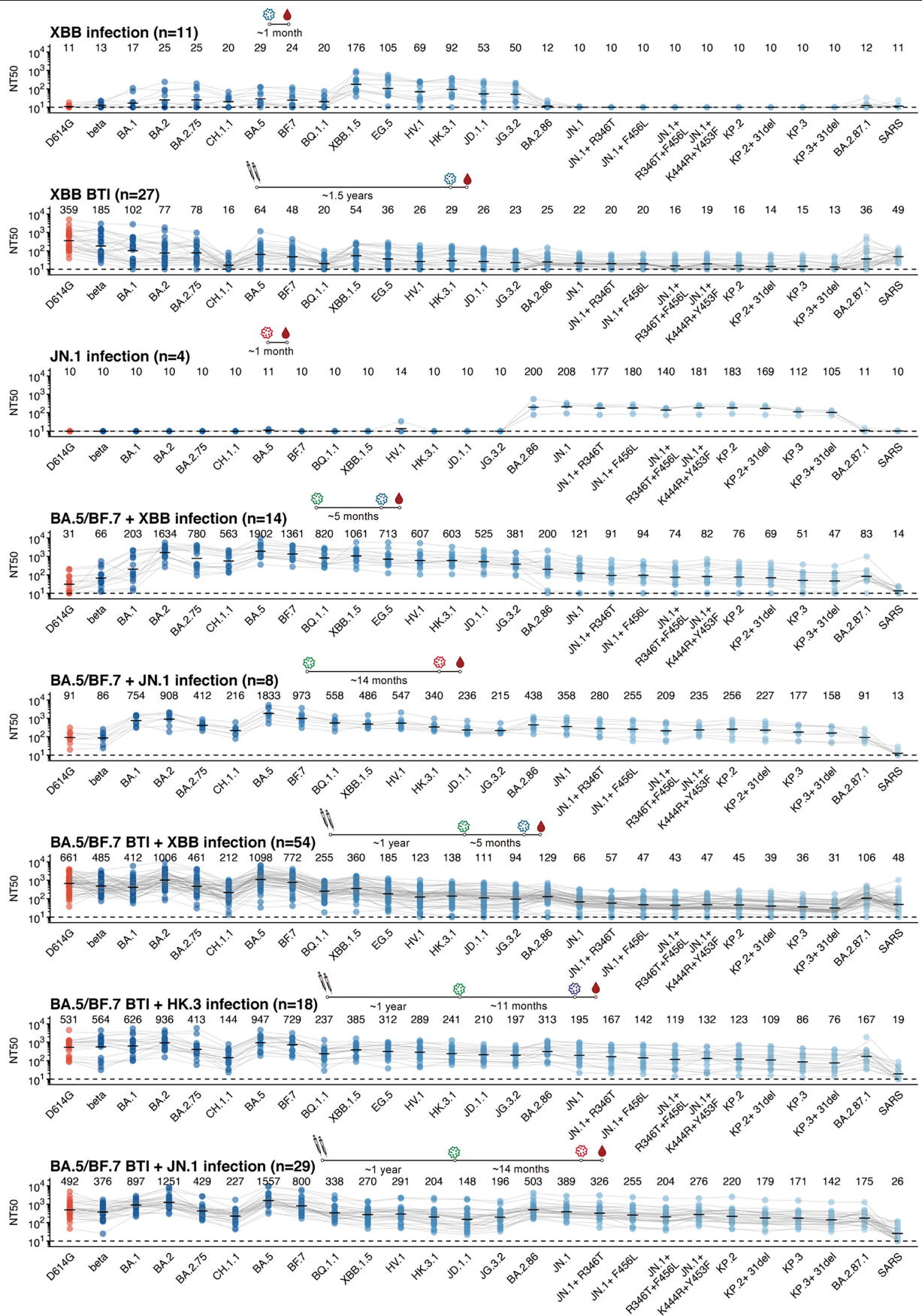
Extended Data Fig. 1 | Prevalence and convergent evolution of JN.1 lineage.

a, Schematic for the convergent evolution of BA.2.86/JN.1 lineage. **b**, Key mutated sites of BA.2.86/JN.1 lineage are indicated on the XBB.1.5 RBD structural model (PDB: 8WRL). **c**, Barplots show the affinities of additional

SARS-CoV-2 variants determined by SPR. **d**, SPR sensorgrams of selected SARS-CoV-2 variants shown in Fig. 1c. Representative results of replicates are shown. Geometric mean k_a , k_d , and K_D of all replicates are labeled.



Extended Data Fig. 2 | Distinct antigenicity of XBB and JN.1 in mice. **a**, Schematic for the mouse immunization experiments. **b**, Radar plots show the serum NT₅₀ of mouse that received 2-dose WT, BA.1, BA.5, XBB, HK.3, BA.2.86, JN.1, KP.2, or SARS-CoV-1 Spike mRNA vaccine against eight representative SARS-CoV-2 variants.

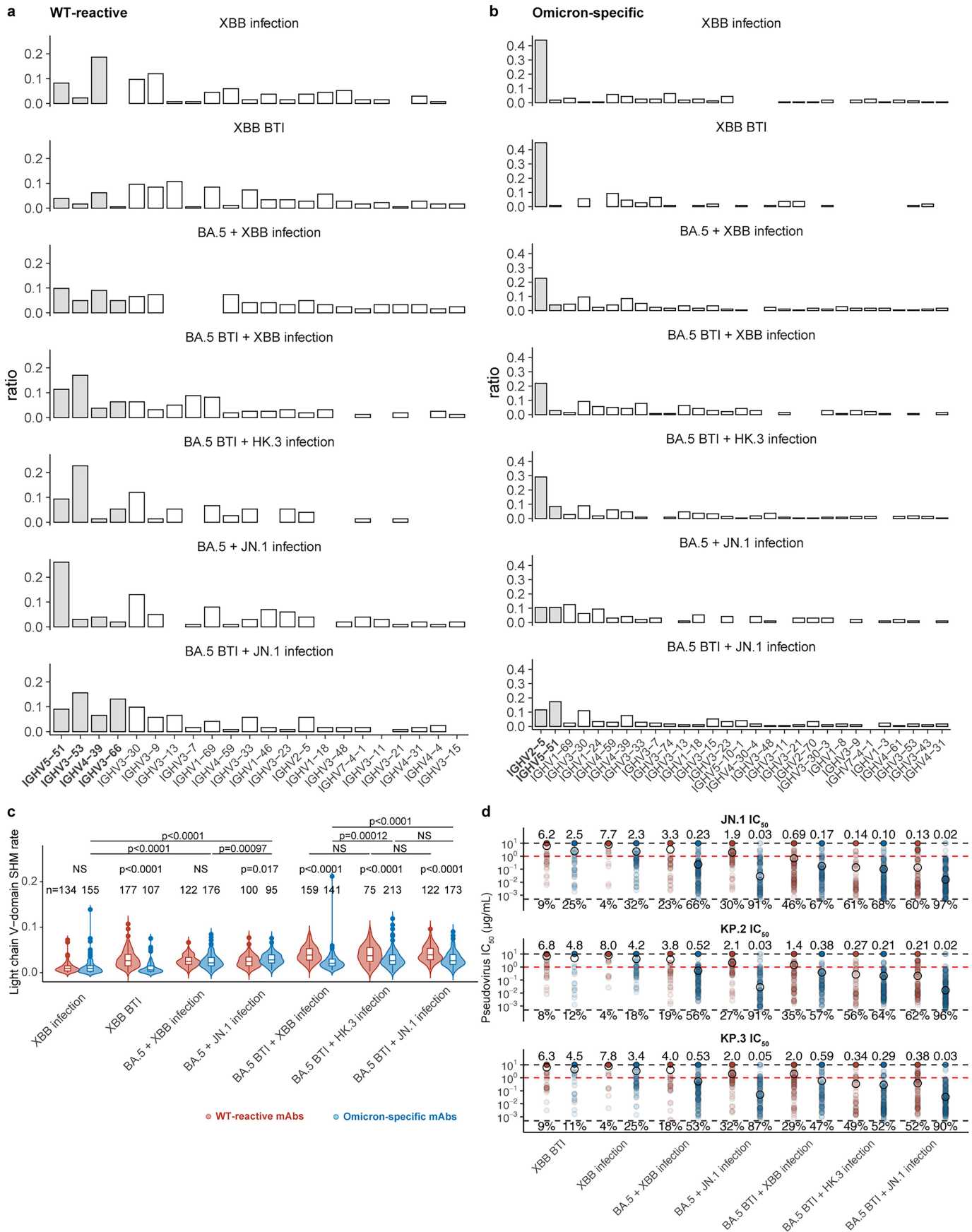


Extended Data Fig. 3 | See next page for caption.

Article

Extended Data Fig. 3 | Plasma neutralization against SARS-CoV-2 variants. NT₅₀ of plasma samples from all of the eight different cohorts against SARS-CoV-2 variant pseudoviruses. Plasma source cohorts and corresponding number of samples, with a schematic showing the immune history, are labeled

above each panel. Dashed lines indicate the limit of detection (NT₅₀ = 10). Numbers of negative samples are labeled below the dashed lines. Geometric mean titers (GMT) values are labeled as black bars and shown above each group of points. Data in Fig. 2 are displayed here again for comparison.



Extended Data Fig. 4 | See next page for caption.

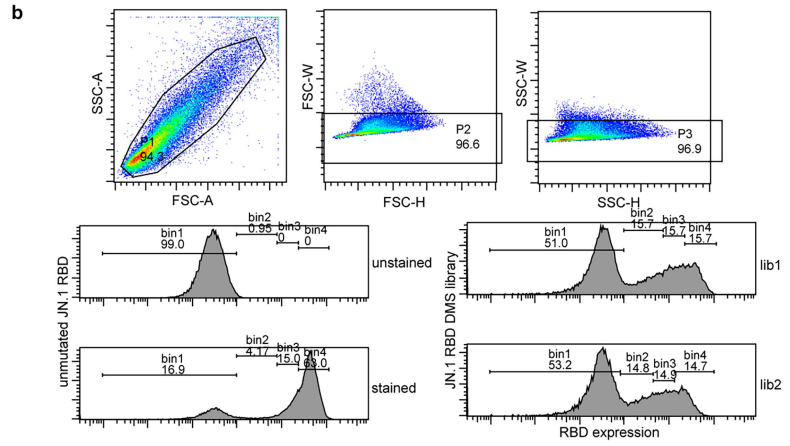
Article

Extended Data Fig. 4 | Properties of WT-reactive and Omicron-specific mAbs. **a-b**, IGHV gene distribution of WT-cross-reactive (**a**) and Omicron-specific (**b**) mAbs isolated from the seven cohorts involved in this study. **c**, Distribution of light chain SHM rate of WT-reactive and Omicron-specific antibodies isolated from different cohorts. Number of mAbs are annotated above each violin plot. Two-tailed Wilcoxon rank-sum tests are used to

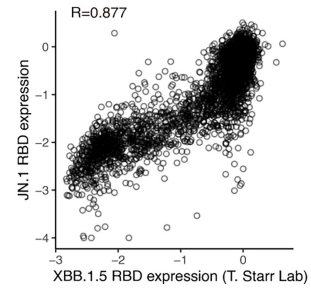
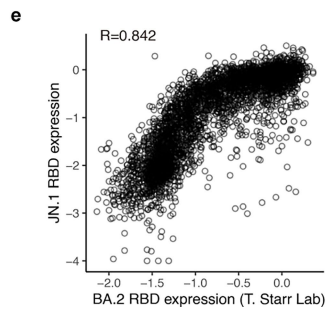
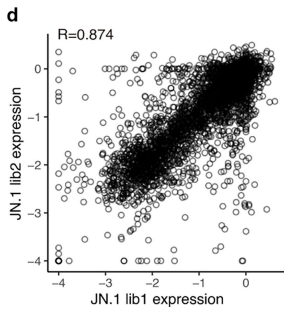
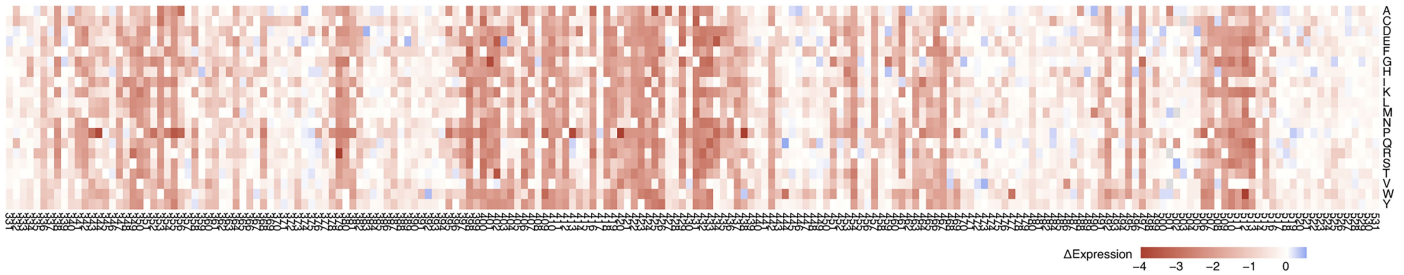
calculate the p-values. NS, not significant. **d**, Neutralization against JN.1, KP.2, and KP.3. Geometric mean IC₅₀ values are shown as circles and annotated above the points. Black dash lines indicate limits of detection (0.005 and 10 µg/mL). Red dashed lines indicate criteria for robust neutralization (1 µg/mL). Percentage of mAbs exhibiting robust neutralization are annotated below the points.

a

antigen	library	variants	detected single mutations
	lib1	180394	4019
XBB.1.5	lib2	122221	4017
	lib1+lib2	302535	4019
	lib1	159928	3994
JN.1	lib2	87824	3994
	lib1+lib2	247679	3999



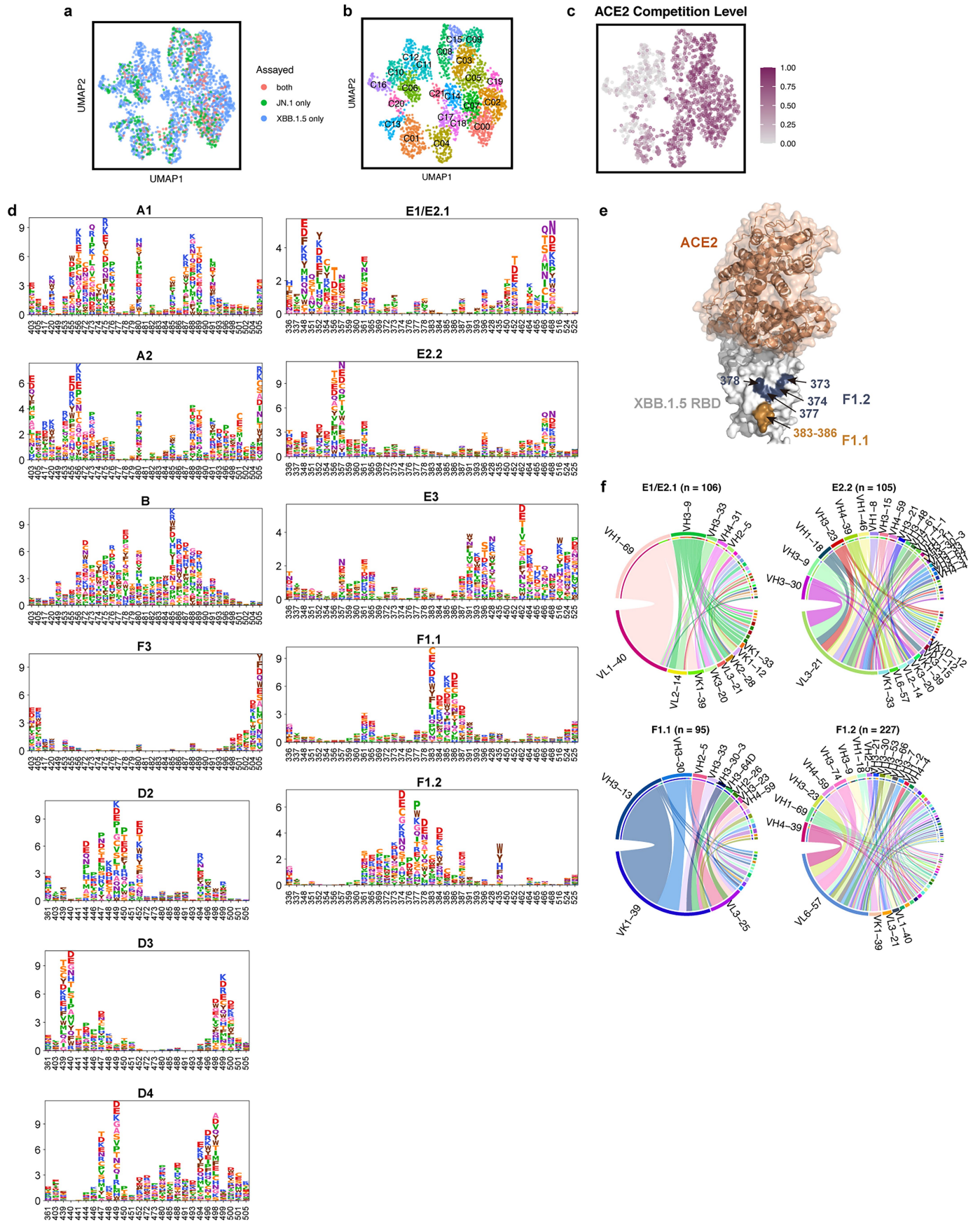
c JN.1 RBD expression (sort-seq)



Extended Data Fig. 5 | Characterization of RBD DMS mutant libraries.

a, Number of variants and detected single mutations in the mutant libraries involved in this study. **b**, FACS diagram for Sort-seq of JN.1 mutant library to determine RBD mutant expression levels. **c**, Heatmap shows the results of DMS

on RBD expression from Sort-seq. **d**, Comparison of RBD expression DMS results from two JN.1 libraries. **e**, Comparison of RBD expression DMS results between JN.1 and BA.2 (left), JN.1 and XBB.1.5 (right).



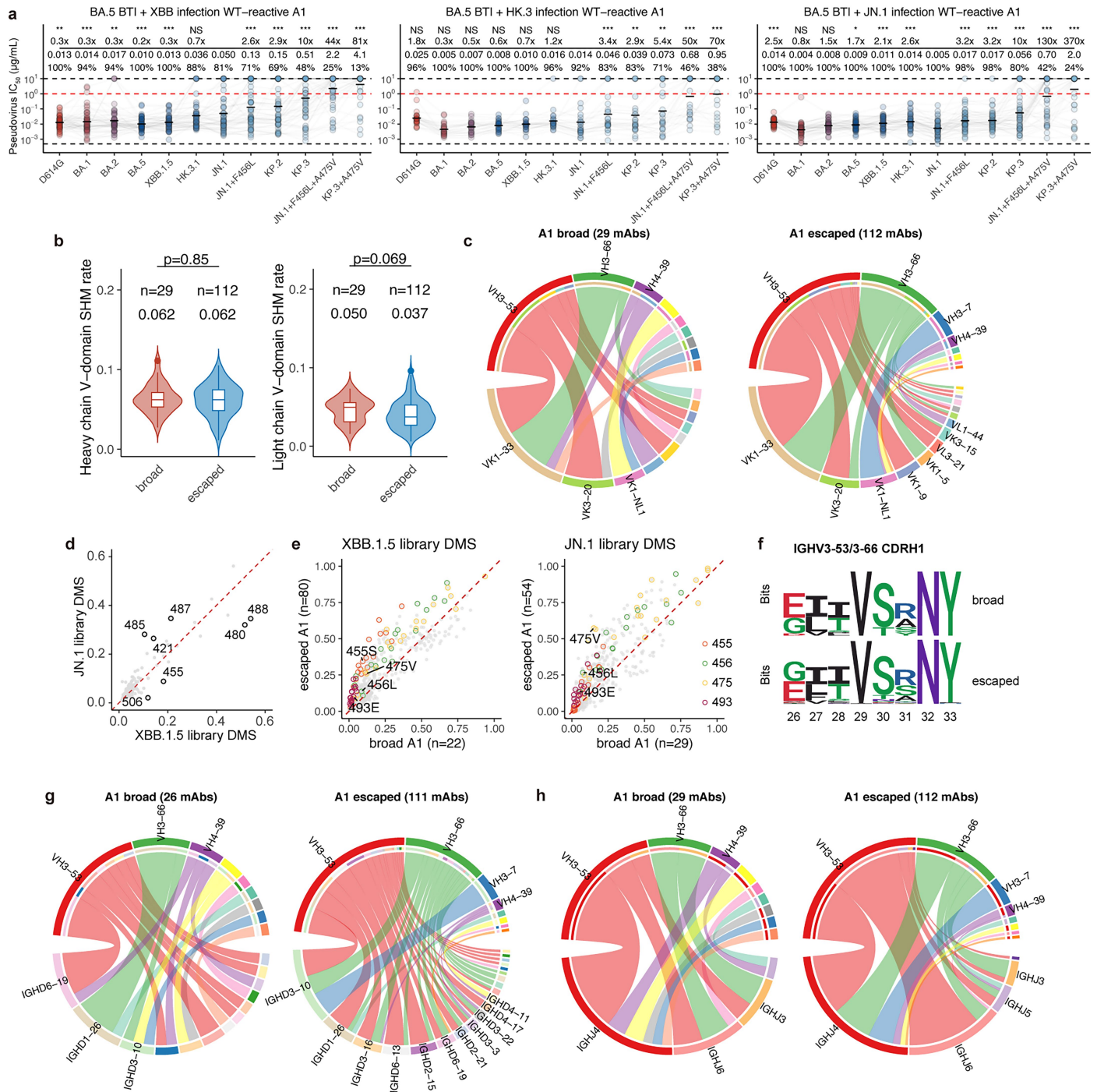
Extended Data Fig. 6 | See next page for caption.

Extended Data Fig. 6 | DMS-based clustering of RBD-specific mAbs.

a, UMAP of mAbs colored by the corresponding RBD basis of DMS experiments. Some mAbs are tested in both antigen mutant libraries and the average results are used for analysis. **b**, Unsupervised clustering of DMS profiles. **c**, UMAP of mAbs colored by ACE2 competition level as determined by competition ELISA. **d**, Logo plots show average escape scores of each RBD mutation of mAbs in

each epitope group. Amino acids are colored according to chemical properties.

e, Structural model of XBB.1.5 RBD in complex of human ACE2 (PDB: 8WRL) with the key residues of epitope groups F1.1 and F1.2 highlighted. **f**, Chord diagram shows the heavy-light chain V gene pairing of mAbs isolated from in epitope groups E1/E2.1, E2.2, F1.1, and F1.2.

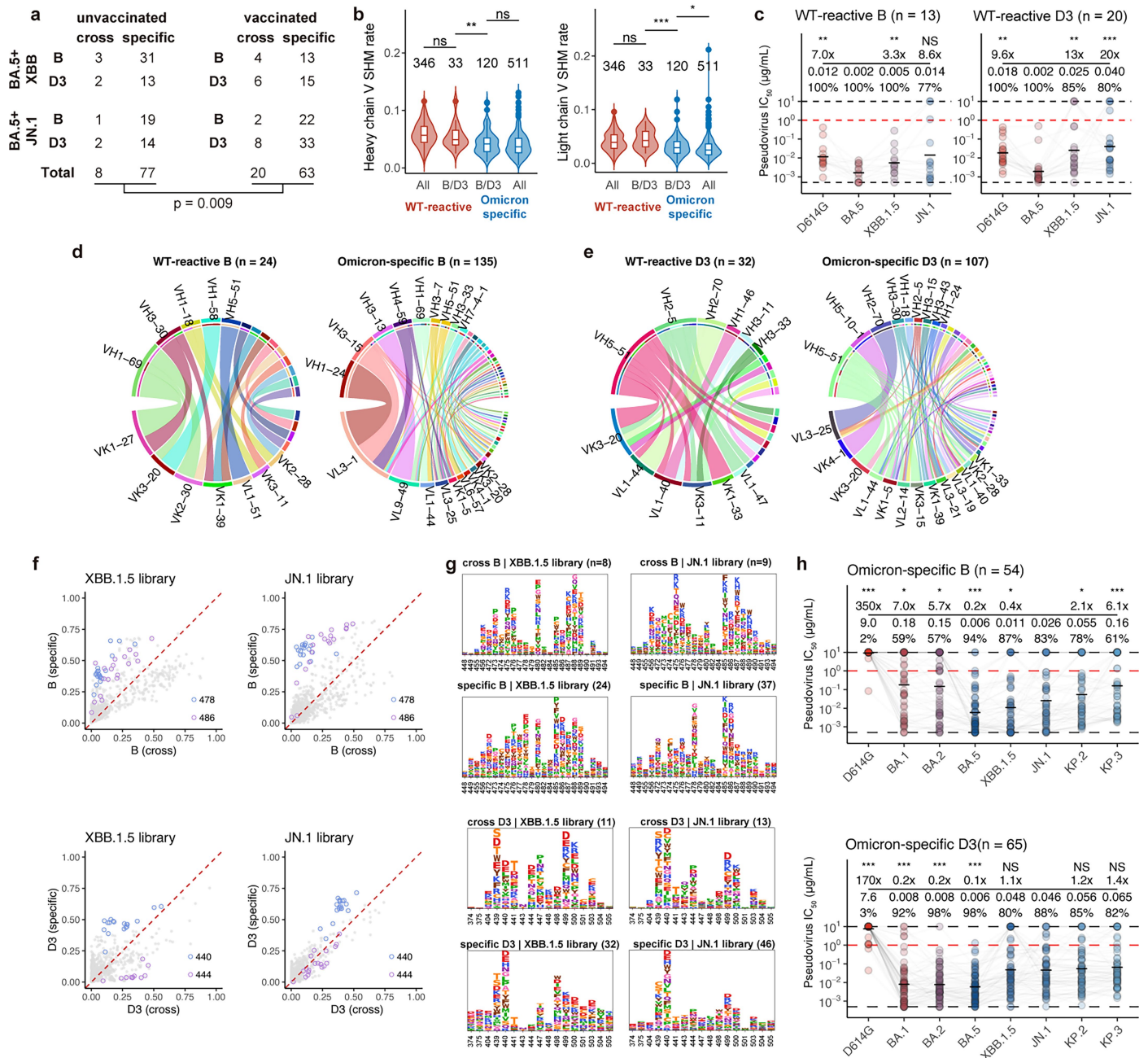


Extended Data Fig. 7 | Properties of WT-reactive mAbs in epitope group A1.

a, Neutralization of WT-reactive mAbs in epitope group A1 from three BTI+ reinfection cohorts against SARS-CoV-2 variants. Geometric mean IC₅₀ values are shown as circles and annotated above the points. Black dash lines indicate limits of detection (0.005 and 10 µg/mL). Red dashed lines indicate criteria for robust neutralization (1 µg/mL). Percentage of mAbs exhibiting robust neutralization, and fold-changes compared to IC₅₀ against JN.1 are annotated above the points. Two-tailed Wilcoxon signed-rank tests are used to determine the p-values. *p < 0.05; **p < 0.01; ***p < 0.001; ****p < 0.0001; NS, not significant.

b, Distribution of SHM rate of WT-reactive broadly neutralizing (broadly against the six tested strains) and escaped A1 antibodies (evaded by at least one variant).

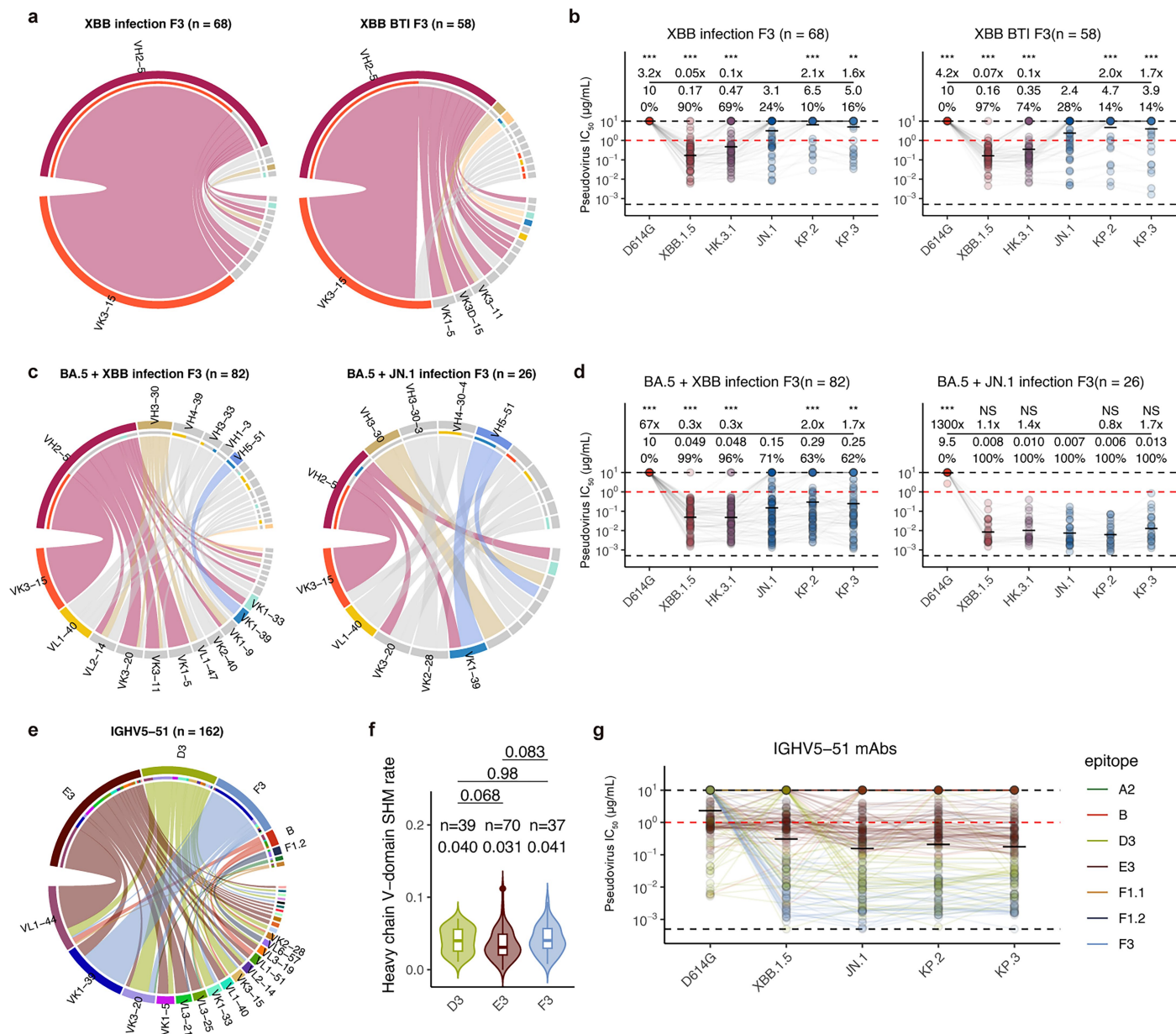
Number of mAbs and median SHM rates are annotated above each violin plot. Two-tailed Wilcoxon rank-sum tests are used to determine the p-values. **c**, Chord diagram shows the heavy-light chain pairing of WT-reactive broadly neutralizing and escaped A1 antibodies. **d**, Comparison of DMS site escape scores using XBB.1.5 library and JN.1 library of mAbs in epitope group A1 which were assayed in both libraries. **e**, Comparison of DMS escape scores of WT-reactive broadly neutralizing and escaped A1 antibodies. **f**, CDR-H1 motifs of IGHV3-53/3-66-encoding WT-reactive broadly neutralizing and escaped A1 antibodies. **g-h**, Chord diagram shows the heavy chain V-D (**g**) or V-J (**h**) pairing of WT-reactive broadly neutralizing and escaped A1 antibodies.



Extended Data Fig. 8 | Properties of mAbs in epitope groups B and D3.

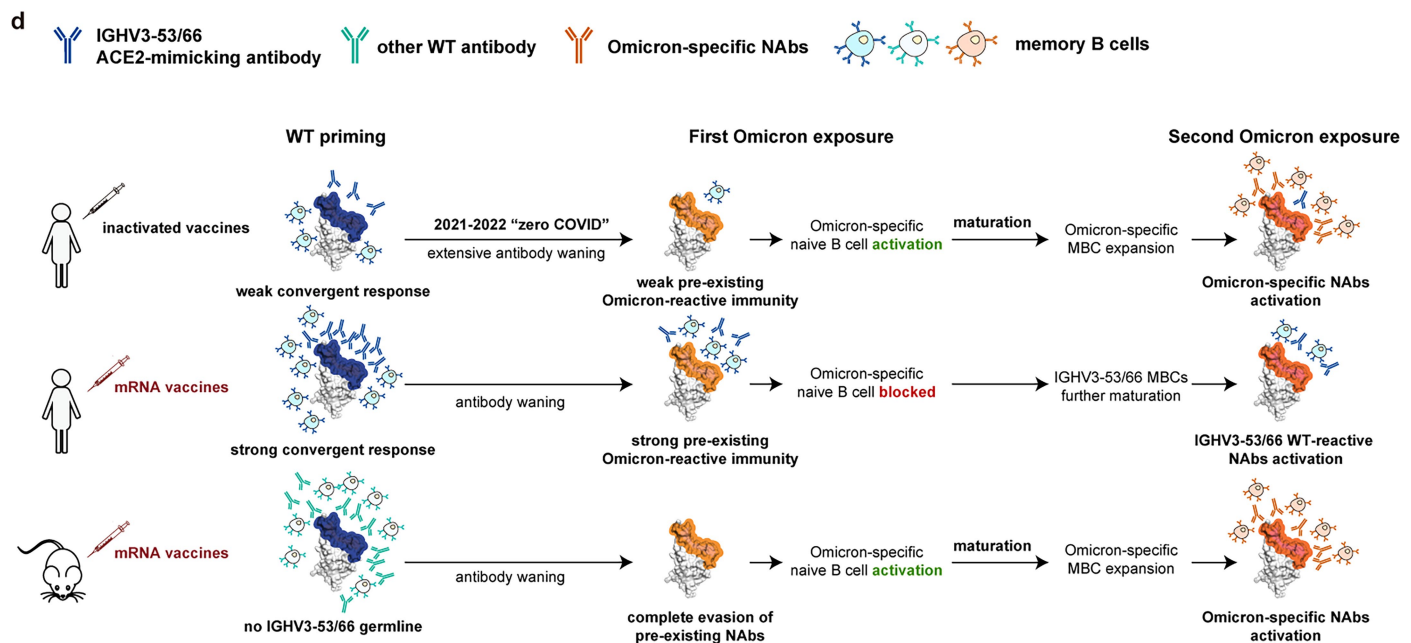
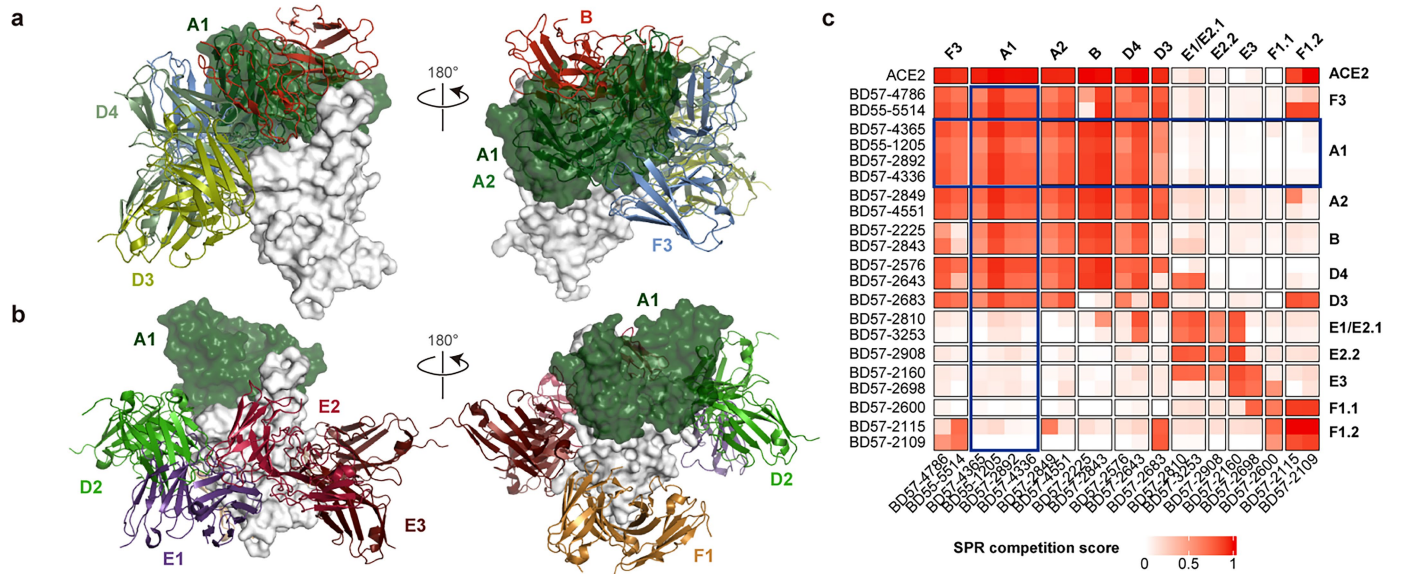
a, Number of WT-cross-reactive and Omicron-specific mAbs in groups B and D3 from vaccinated and corresponding unvaccinated cohorts. The p-values are calculated using two-tailed hypergeometric test. **b**, Distribution of SHM rate of WT-reactive and Omicron-specific B/D3 antibodies. Number of mAbs are annotated above each violin plot. Two-tailed Wilcoxon rank-sum tests are used to determine the p-values. * $p < 0.05$; ** $p < 0.01$; *** $p < 0.001$; **** $p < 0.0001$; ns, not significant. **c**, Neutralization of WT-reactive B and D3 mAbs against D614G, BA.5, XBB.1.5, and JN.1. Percentage of mAbs exhibiting robust neutralization, and fold-changes compared to IC_{50} against BA.5 are annotated above the

points. **d-e**, Chord diagram shows the heavy-light chain pairing of WT-reactive and Omicron-specific B (**d**) or D3 (**e**) mAbs. **f-g**, Scatter plots (**f**) and logo plots (**g**) to compare the DMS escape scores of WT-reactive (cross) and Omicron-specific B/D3 mAbs. **h**, Neutralization of Omicron-specific B and D3 mAbs against SARS-CoV-2 variant pseudovirus. Black dash lines indicate limits of detection (0.005 and 10 $\mu\text{g/mL}$). Red dashed lines indicate criteria for robust neutralization (1 $\mu\text{g/mL}$). Percentage of mAbs exhibiting robust neutralization, and fold-changes compared to IC_{50} against JN.1 are annotated above the points. Two-tailed Wilcoxon signed-rank tests are used to determine the p-values. * $p < 0.05$; ** $p < 0.01$; *** $p < 0.001$; NS, not significant.



Extended Data Fig. 9 | Properties of F3 and IGHV5-51 mAbs. **a**, Chord diagram shows the heavy-light chain pairing of F3 mAbs elicited by XBB infection (left) and XBB BTI (right). **b**, Neutralization of F3 mAbs elicited by XBB infection (left) and XBB BTI (right) against SARS-CoV-2 variant pseudovirus. **c**, Chord diagram shows the heavy-light chain pairing of F3 mAbs elicited by BA.5 + XBB infection (left) and BA.5 + JN.1 infection (right). **d**, Neutralization of F3 mAbs

elicited by BA.5 + XBB infection (left) and BA.5 + JN.1 infection (right) against SARS-CoV-2 variant pseudovirus. **e**, Relationship between light chain V genes and epitope groups of IGHV5-51-encoding mAbs. **f**, Comparison of heavy chain SHM rates of IGHV5-51-encoding mAbs in epitope groups D3, E3, and F3. **g**, Neutralization of IGHV5-51-encoding mAbs in various epitope groups against D614G, XBB.1.5, JN.1, KP.2, and KP.3 pseudovirus.



Extended Data Fig. 10 | Competition between Class 1 and Omicron-specific NAbs. **a**, Superimposed structural models of representative antibodies in epitope group A1 and Omicron-specific neutralizing epitope groups. **b**, Superimposed structural models of representative antibodies in epitope group A1 and WT-reactive epitope groups. **c**, Heatmap for pair-wised SPR

competition scores of representative mAbs in various epitope groups on XBB.1.5 RBD. Results related to epitope group A1 are highlighted by blue rectangles. **d**, Schematic for the model to explain the mRNA vaccine-induced immune imprinting.

Reporting Summary

Nature Portfolio wishes to improve the reproducibility of the work that we publish. This form provides structure for consistency and transparency in reporting. For further information on Nature Portfolio policies, see our [Editorial Policies](#) and the [Editorial Policy Checklist](#).

Statistics

For all statistical analyses, confirm that the following items are present in the figure legend, table legend, main text, or Methods section.

- | | |
|-------------------------------------|--|
| n/a | Confirmed |
| <input type="checkbox"/> | <input checked="" type="checkbox"/> The exact sample size (n) for each experimental group/condition, given as a discrete number and unit of measurement |
| <input type="checkbox"/> | <input checked="" type="checkbox"/> A statement on whether measurements were taken from distinct samples or whether the same sample was measured repeatedly |
| <input type="checkbox"/> | <input checked="" type="checkbox"/> The statistical test(s) used AND whether they are one- or two-sided
<i>Only common tests should be described solely by name; describe more complex techniques in the Methods section.</i> |
| <input checked="" type="checkbox"/> | <input type="checkbox"/> A description of all covariates tested |
| <input checked="" type="checkbox"/> | <input type="checkbox"/> A description of any assumptions or corrections, such as tests of normality and adjustment for multiple comparisons |
| <input type="checkbox"/> | <input checked="" type="checkbox"/> A full description of the statistical parameters including central tendency (e.g. means) or other basic estimates (e.g. regression coefficient) AND variation (e.g. standard deviation) or associated estimates of uncertainty (e.g. confidence intervals) |
| <input type="checkbox"/> | <input checked="" type="checkbox"/> For null hypothesis testing, the test statistic (e.g. F , t , r) with confidence intervals, effect sizes, degrees of freedom and P value noted
<i>Give P values as exact values whenever suitable.</i> |
| <input checked="" type="checkbox"/> | <input type="checkbox"/> For Bayesian analysis, information on the choice of priors and Markov chain Monte Carlo settings |
| <input checked="" type="checkbox"/> | <input type="checkbox"/> For hierarchical and complex designs, identification of the appropriate level for tests and full reporting of outcomes |
| <input checked="" type="checkbox"/> | <input type="checkbox"/> Estimates of effect sizes (e.g. Cohen's d , Pearson's r), indicating how they were calculated |

Our web collection on [statistics for biologists](#) contains articles on many of the points above.

Software and code

Policy information about [availability of computer code](#)

Data collection	Pseudovirus neutralization and ELISA data were collected by Multiskan™ FC Microplate Photometer. SPR data was collected by BIAcore 8K Evaluation Software (v4.0.8.20368; GE Healthcare). FACS data was collected by Summit 6.0 (Beckman Coulter).
Data analysis	Neutralization assays data were analyzed using PRISM (v9.0.1) . FACS data were analyzed by FlowJo 10.8. SPR data were analyzed by BIAcore 8K Evaluation Software ((v4.0.8.20368; Cytiva). Sequence alignment of Omicron sublineages was performed by biopython (v1.78); V(D)J sequence data were aligned using Cell Ranger (v6.1.1), The IgBlast program (v1.17.1) and Change-O toolkit (v1.2.0) were utilized to annotate the germline V(D)J genes and detect somatic hypermutation sites in the variable domain of the BCR sequences. Illumina barcodes sequencing data from deep mutational scanning experiments were analyzed using custom scripts (https://github.com/jianfcpku/SARS-CoV-2-reinfection-DMS) and Python package dms_variants (v0.8.9). Custom scripts to analyze the escape mutation profiles data are available at Github (https://github.com/yunlongcaolab/SARS-CoV-2-JN.1-mAbs). We used Python package logomaker (v0.8), R package ggseqlogo (v0.1) and ggplot2 (v3.3.3) for illustration, and Python package python-igraph (v0.9.6), scipy (v1.7.0), scikit-learn (v0.24.2), leidenalg (v0.8.7), umap-learn (v0.5.2) to perform clustering and UMAP.

For manuscripts utilizing custom algorithms or software that are central to the research but not yet described in published literature, software must be made available to editors and reviewers. We strongly encourage code deposition in a community repository (e.g. GitHub). See the Nature Portfolio [guidelines for submitting code & software](#) for further information.

Data

Policy information about [availability of data](#)

All manuscripts must include a [data availability statement](#). This statement should provide the following information, where applicable:

- Accession codes, unique identifiers, or web links for publicly available datasets
- A description of any restrictions on data availability
- For clinical datasets or third party data, please ensure that the statement adheres to our [policy](#)

DMS data and custom scripts can be downloaded at Zenodo (doi: 10.5281/zenodo.13893217) and Github (<https://github.com/yunlongcaolab/SARS-CoV-2-JN.1-mAbs>). Information of the mAbs involved in this study are included in Supplementary Table 2. We used vdj_GRCh38_alts_ensembl-5.0.0 as the reference of V(D)J alignment, which can be obtained from <https://support.10xgenomics.com/single-cell-vdj/software/downloads/latest>. PDB 8WRL is used for the structural model of SARS-CoV-2 XBB.1.5 RBD.

Field-specific reporting

Please select the one below that is the best fit for your research. If you are not sure, read the appropriate sections before making your selection.

Life sciences Behavioural & social sciences Ecological, evolutionary & environmental sciences

For a reference copy of the document with all sections, see [nature.com/documents/nr-reporting-summary-flat.pdf](https://www.nature.com/documents/nr-reporting-summary-flat.pdf)

Life sciences study design

All studies must disclose on these points even when the disclosure is negative.

Sample size	A total of 2000 monoclonal antibodies were produced and characterized in the manuscript. We analyzed all antibodies in hand and the sample size of antibodies in this study was sufficient to reach statistical significance by Wilcoxon rank-sum tests for the differences in SHM rates of mAbs from different cohorts and with different specificities. We collected plasma samples from 54 convalescent individuals with BA.5/BF.7 BTI and XBB infection, 27 with XBB BTI, 18 BA.5/BF.7 BTI and HK.3 infection, and 29 with BA.5/BF.7 BTI + JN.1 infection. Further, we investigated 14 individuals with BA.5/BF.7 and XBB infection, 8 BA.5/BF.7 and JN.1 infection, 11 with XBB infection, and 4 with JN.1 infection, who had no history of vaccination. We immunized 10 mice for each group in animal studies. We analyzed all plasma samples collected and the sample size of plasma could reach statistical significance of NT50 values from neutralization assays by two-tailed Wilcoxon signed-rank test. No sample size calculation was performed.
Data exclusions	51 antibodies were excluded from the statistical analyses due to lack of specificity to at least one of SARS-CoV-2 variant RBD. No plasma sample was excluded from the study.
Replication	Experimental assays were performed in at least two independent experiments according to or exceeding standards in the field. Specifically, we performed mutation screening using two independently constructed mutant libraries. We conducted all neutralization assays, ELISA, and SPR assays in at least two independent experiments. Representative results of replicates are reported.
Randomization	Randomization was not required since we were applying a uniform set of measurements across the panel of monoclonal antibodies and plasma. As this is an observational study, randomization is not relevant.
Blinding	Blinding was not required since we were applying a uniform set of measurements across the panel of monoclonal antibodies and plasma. As this is an observational study, investigators were not blinded.

Reporting for specific materials, systems and methods

We require information from authors about some types of materials, experimental systems and methods used in many studies. Here, indicate whether each material, system or method listed is relevant to your study. If you are not sure if a list item applies to your research, read the appropriate section before selecting a response.

Materials & experimental systems

n/a	<input type="checkbox"/>	Involvement in the study
<input type="checkbox"/>	<input checked="" type="checkbox"/>	Antibodies
<input type="checkbox"/>	<input checked="" type="checkbox"/>	Eukaryotic cell lines
<input checked="" type="checkbox"/>	<input type="checkbox"/>	Palaeontology and archaeology
<input type="checkbox"/>	<input checked="" type="checkbox"/>	Animals and other organisms
<input type="checkbox"/>	<input checked="" type="checkbox"/>	Human research participants
<input checked="" type="checkbox"/>	<input type="checkbox"/>	Clinical data
<input checked="" type="checkbox"/>	<input type="checkbox"/>	Dual use research of concern

Methods

n/a	<input type="checkbox"/>	Involvement in the study
<input checked="" type="checkbox"/>	<input type="checkbox"/>	ChIP-seq
<input type="checkbox"/>	<input checked="" type="checkbox"/>	Flow cytometry
<input checked="" type="checkbox"/>	<input type="checkbox"/>	MRI-based neuroimaging

Antibodies

Antibodies used

ELISA: 0.25 µg/ml goat anti-human IgG(H+L)HRP (JACKSON, 109-035-003)
 1 µg/ml H7N9 human IgG1 antibody HG1K (Sino Biologicals, Cat #HG1K) was used as negative control.
 FACS: The cells were stained with FITC anti-human CD20 antibody (BioLegend, 302304), Brilliant Violet 421 anti-human CD27 antibody (BioLegend, 302824), PE/Cyanine7 anti-human IgM antibody (BioLegend, 314532), PE/Cyanine7 anti-human IgD antibody (BioLegend, 348210).
 All human antibodies were expressed using Expi293F™ (Gibco, A14527) with codon-optimized cDNA and human IgG1 constant regions in house. The detailed sequence could be found in Supplementary material.

Validation

All antibodies were expressed using Expi293F™ with codon-optimized cDNA and human IgG1 constant regions. All antibodies' species and specificity to RBD were validated by ELISA. All antibodies neutralization ability was verified by VSV-based pseudotyped virus assays. Details for all SARS-CoV-2 antibodies evaluated in this study is included in Supplementary Table 2.
 Goat anti-human IgG(H+L)HRP (JACKSON, 109-035-003): Based on immunoelectrophoresis and/or ELISA, the antibody reacts with whole molecule human IgG. It also reacts with the light chains of other human immunoglobulins. No antibody was detected against non-immunoglobulin serum proteins. The antibody may cross-react with immunoglobulins from other species.
 FITC anti-human CD20 antibody was validated by successful staining and FC analysis according to the manufacturer's website <https://www.biolegend.com/en-us/products/fic-anti-human-cd20-antibody-558> and previous publication: Mishra A, et al. 2021. Cell 184(13):3394-3409.e20
 Brilliant Violet 421 anti-human CD27 antibody was validated by successful staining and FC analysis according to the manufacturer's website <https://www.biolegend.com/en-us/products/brilliant-violet-421-anti-human-cd27-antibody-7276> and previous publication Dugan HL, et al. 2021. Immunity. 54(6):1290-1303
 PE/Cyanine7 anti-human IgM antibody was validated by successful staining and FC analysis according to the manufacturer's website <https://www.biolegend.com/en-us/products/pe-cyanine7-anti-human-igm-antibody-12467> and previous publication: Shehata L, et al 2019. Nat Commun. 10:1126
 PE/Cyanine7 anti-human IgD antibody was validated by successful staining and FC analysis according to the manufacturer's website <https://www.biolegend.com/en-us/products/pe-cyanine7-anti-human-igd-antibody-6996> and previous publication: Ahmed R et al. 2019. Cell. 177(6):1583-1599.

Eukaryotic cell lines

Policy information about cell lines

Cell line source(s)

Monoclonal antibody expression: Expi293F™ (Gibco, A14527);
 Yeast display: EBY100 (ATCC MYA-4941);
 Pseudotyped virus neutralization assay: Huh-7 (JCRB 0403) ;
 Authentic virus neutralizing assay: Vero(ATCC CCL-81);
 293T(ATCC, CRL-3216);

Authentication

Expi293F™ (Gibco, A14527): Morphology(https://www.thermofisher.com/document-connect/document-connect.html?url=https://assets.thermofisher.com/TFS-Assets%2Fcertificate%2FFRK%2FCOA%2FCOA_100044202_275162_1.pdf);
 EBY100 (ATCC MYA-4941): Whole-genome Sequencing(<https://www.atcc.org/products/mya-4941>);
 Huh-7 (JCRB 0403): Morphology(https://cellbank.nibiohn.go.jp/~cellbank/en/search_res_det.cgi?ID=385);
 Vero(ATCC CCL-81): Morphology(<https://www.atcc.org/products/ccl-81#related-products>);
 293T(ATCC, CRL-3216): STR profiling(<https://www.atcc.org/products/crl-3216>)

Mycoplasma contamination

Not tested for mycoplasma contamination;

Commonly misidentified lines
(See [ICLAC](https://www.thermofisher.com/ICLAC) register)

No commonly misidentified cell lines were used in the study.

Animals and other organisms

Policy information about [studies involving animals](#); [ARRIVE guidelines](#) recommended for reporting animal research

Laboratory animals	Female, six to eight-week-old BALB/c mice were used in this study
Wild animals	No wild animals were used.
Field-collected samples	No field-collected samples were used.
Ethics oversight	Animal experiments were carried out under study protocols approved by Institute of Biophysics, Chinese Academy of Sciences (SYXK2023300) and HFK Biologics (HFK-AP-20210930).

Note that full information on the approval of the study protocol must also be provided in the manuscript.

Human research participants

Policy information about [studies involving human research participants](#)

Population characteristics	We collected plasma samples from 54 convalescent individuals with BA.5/BF.7 B.1.1.7 infection, 27 with XBB B.1.1.5 infection, 18 BA.5/BF.7 B.1.1.7 and HK.3 B.1.1.7 infection, and 29 with BA.5/BF.7 B.1.1.7 + JN.1 B.1.1.7 infection. Further, we investigated 14 individuals with BA.5/BF.7 and XBB B.1.1.5 infection, 8 BA.5/BF.7 and JN.1 B.1.1.7 infection, 11 with XBB B.1.1.5 infection, and 4 with JN.1 B.1.1.7 infection, who had no history of vaccination. The gender, age, vaccination status, infection time, and sampling time were listed in Supplementary Table 1.
Recruitment	Patients were recruited on the basis of SARS-CoV-2 vaccinations, and known SARS-CoV-2 infections indicated by SARS-CoV-2 PCR or antigen tests. The strains that infected the participants were inferred from corresponding regional epidemiological data, as described in the online methods. The exclusion criteria for the study included individuals with HIV or other debilitating diseases, as well as immunocompromised individuals.
Ethics oversight	Blood samples from vaccinated or unvaccinated individuals were obtained under study protocols approved by Beijing Ditan Hospital, Capital Medical University (Ethics committee archiving No. LL-2021-024-02) and the Tianjin Municipal Health Commission, and the Ethics Committee of Tianjin First Central Hospital (Ethics committee archiving No. 2022N045KY). All participants have provided written informed consent for the collection of information, storage and use of their clinical samples for research purposes, and publication of data generated from this study.

Note that full information on the approval of the study protocol must also be provided in the manuscript.

Flow Cytometry

Plots

Confirm that:

- The axis labels state the marker and fluorochrome used (e.g. CD4-FITC).
- The axis scales are clearly visible. Include numbers along axes only for bottom left plot of group (a 'group' is an analysis of identical markers).
- All plots are contour plots with outliers or pseudocolor plots.
- A numerical value for number of cells or percentage (with statistics) is provided.

Methodology

Sample preparation	Whole blood sample were diluted 1:1 with PBS+2% FBS (Gibco) and subjected to Ficoll (Cytiva) gradient centrifugation. Plasma was collected from upper layer. Cells were collected at the interface and further prepared by centrifugation, red blood cells lysis (Invitrogen eBioscience) and washing steps. Samples were stored in FBS (Gibco) with 10% DMSO (Sigma) in liquid nitrogen if not used for downstream process immediately. Cryopreserved PBMCs were thawed in PBS+2% FBS. CD19+ B cells were enriched from PBMCs using EasySep Human CD19 Positive Selection Kit II (STEMCELL, 17854). Following enrichment, 1×10^6 B cells in 100 μ l buffer were incubated with a panel of antibodies including 3 μ l FITC anti-human CD20 antibody (BioLegend, 302304), 3.5 μ l Brilliant Violet 421 anti-human CD27 antibody (BioLegend, 302824), 2 μ l PE/Cyanine7 anti-human IgD antibody (BioLegend, 348210) and 2 μ l PE/Cyanine7 anti-human IgM antibody (BioLegend, 314532). Additionally, fluorophore or oligonucleotide conjugated RBD were added. For FACS, 0.013 μ g of biotinylated XBB.1.5, HK.3, or JN.1 RBD protein (customized from Sino Biological) conjugated with PE-streptavidin (BioLegend, 405204) and APC-streptavidin (BioLegend, 405207), and 0.013 μ g of WT biotinylated RBD protein (Sino Biological, 40592-V27H-B) conjugated with BV605-streptavidin (BioLegend, 405229) were added. For sequencing, XBB.1.5, HK.3, or JN.1 biotinylated RBD protein conjugated with TotalSeq™-C0971 Streptavidin (BioLegend, 405271) and TotalSeq™-C0972 Streptavidin (BioLegend, 405273), WT biotinylated RBD protein conjugated with TotalSeq™-C0973 Streptavidin (BioLegend, 405275) and TotalSeq™-C0974 Streptavidin (BioLegend, 405277) and biotinylated Ovalbumin (Sino Biological) conjugated with TotalSeq™-C0975 Streptavidin (BioLegend, 405279) were added. After incubation and washing steps, 5 μ l of 7-AAD (Invitrogen, 00-6993-50) was included for dead cell exclusion.
Instrument	Moflo Astrios EQ (BeckMan Coulter)

Software	Summit 6.0 (Beckman Coulter) for cell sorting; FlowJo 10.8 for data analysis.
Cell population abundance	Detailed abundance data are shown in the Supplementary Information.
Gating strategy	Cells negative for 7-AAD, IgM and IgD, but positive for CD20, CD27 and XBB.1.5, HK.3 or JN.1 RBD were sorted, the gating strategy is provided in the Supplementary Information

Tick this box to confirm that a figure exemplifying the gating strategy is provided in the Supplementary Information.